The Astrophysical Journal, 943:166 (27pp), 2023 February 1 https://doi.org/10.3847/1538-4357/aca294

Beyond UVJ: Color Selection of Galaxies in the JWST Era

Jacqueline Antwi-Danso[1,2], Casey Papovich[1,2], Joel Leja[3,4,5], Danilo Marchesini[6], Z. Cemile Marsan[7], Nicholas S. Martis[8,9], Ivo Labbé[10], Adam Muzzin[7], Karl Glazebrook[10], Caroline M. S. Straatman[11,12], and Kim-Vy H. Tran[13,14]

[1] George P. and Cynthia Woods Mitchell Institute for Fundamental Physics and Astronomy, Texas A&M University, College Station, TX 77840, USA
jadanso@tamu.edu
[2] Department of Physics and Astronomy, Texas A&M University, 4242 TAMU, College Station, TX 77840, USA
[3] Department of Astronomy & Astrophysics, The Pennsylvania State University, University Park, PA 16802, USA
[4] Institute for Computational & Data Sciences, The Pennsylvania State University, University Park, PA 16802, USA
[5] Institute for Gravitation and the Cosmos, The Pennsylvania State University, University Park, PA 16802, USA
[6] Department of Physics and Astronomy, Tufts University, Medford, MA 02155, USA
[7] Department of Physics and Astronomy, York University, Toronto, Ontario, ON M3J 1P3, Canada
[8] Department of Astronomy and Physics, St. Mary's University, Halifax, Nova Scotia, NS B3H 3C3, Canada
[9] National Research Council of Canada, Herzberg Astronomy & Astrophysics Research Centre, 5071 West Saanich Road, Victoria, BC, V9E 2E7, Canada
[10] Center for Astrophysics & Supercomputing, Swinburne University, Hawthorn, Victoria, 3122, Australia
[11] Department of Physics and Astronomy, Ghent University, Krijgslaan 281 S9, B-9000 Gent, Belgium
[12] Max-Planck Institut für Astronomie, Königstuhl 17, D-69117, Heidelberg, Germany
[13] School of Physics, University of New South Wales, Kensington, 2052, Australia
[14] ARC Centre for Excellence in All-Sky Astrophysics in 3D, 2611, Australia
Received 2022 July 12; revised 2022 November 4; accepted 2022 November 11; published 2023 February 6

Abstract

We present a new rest-frame color–color selection method using synthetic $u_s - g_s$ and $g_s - i_s$, $(ugi)_s$ colors to identify star-forming and quiescent galaxies. Our method is similar to the widely used $U - V$ versus $V - J$ (*UVJ*) diagram. However, *UVJ* suffers known systematics. Spectroscopic campaigns have shown that *UVJ*-selected quiescent samples at $z \gtrsim 3$ include ∼10%–30% contamination from galaxies with dust-obscured star formation and strong emission lines. Moreover, at $z > 3$, *UVJ* colors are extrapolated because the rest-frame band shifts beyond the coverage of the deepest bandpasses at $<5\ \mu$m (typically Spitzer/IRAC 4.5 μm or future JWST/NIRCam observations). We demonstrate that $(ugi)_s$ offers improvements to *UVJ* at $z > 3$, and can be applied to galaxies in the JWST era. We apply $(ugi)_s$ selection to galaxies at $0.5 < z < 6$ from the (observed) 3D-HST and UltraVISTA catalogs, and to the (simulated) JAGUAR catalogs. We show that extrapolation can affect $(V - J)_0$ color by up to 1 mag, but changes $(g_s - i_s)_0$ color by $\leqslant 0.2$ mag, even at $z \simeq 6$. While $(ugi)_s$-selected quiescent samples are comparable to *UVJ* in completeness (both achieve ∼85%–90% at $z = 3$–3.5), $(ugi)_s$ reduces contamination in quiescent samples by nearly a factor of 2, from ≃35% to ≃17% at $z = 3$, and from ≃60% to ≃33% at $z = 6$. This leads to improvements in the true-to-false-positive ratio (TP/FP), where we find TP/FP $\gtrsim 2.2$ for $(ugi)_s$ at $z \simeq 3.5 - 6$, compared to TP/FP < 1 for *UVJ*-selected samples. This indicates that contaminants will outnumber true quiescent galaxies in *UVJ* at these redshifts, while $(ugi)_s$ will provide higher-fidelity samples.

Unified Astronomy Thesaurus concepts: Galaxy photometry (611); High-redshift galaxies (734); Catalogs (205); Surveys (1671)

1. Introduction

Over the past two decades, deep extragalactic surveys have yielded impressive numbers of galaxies in the high-redshift universe, thereby improving our understanding of galaxy evolution. The development of sensitive near-infrared (NIR) imagers such as Magellan/FourStar (Persson et al. 2013), Very Large Telescope (VLT)/HAWK-I (Kissler-Patig et al. 2008), ESO/VISTA (Sutherland et al. 2015), and UKIRT/WFCAM (Casali et al. 2007) and their incorporation into multiwavelength surveys have yielded thousands of galaxy candidates at $z = 3$–6. The addition of medium-band filters with deep NIR surveys such as NMBS (Whitaker et al. 2011) and ZFOURGE (Straatman et al. 2016) has additionally improved the color selection of galaxies at these redshifts, enabling the detection and characterization of red galaxies over cosmic time (e.g., Marchesini et al. 2010; Spitler et al. 2014; Straatman et al. 2014; Patel et al. 2017). Using these data, we have demonstrated that we can accurately determine redshifts and distinguish between star-forming and quiescent galaxies with photometric data alone. Similarly, surveys of deep fields and lensing clusters using the Hubble Space Telescope (HST) have revealed hundreds of galaxies and galaxy candidates at $z = 7$–10, enabling us to identify and characterize some of the very first sources in the universe (Grogin et al. 2011; Koekemoer et al. 2011; Bradley et al. 2012; Ellis et al. 2013; Bradley et al. 2014; Schmidt et al. 2014; Lotz et al. 2017; Salmon et al. 2018; Coe et al. 2019).

The recently launched James Webb Space Telescope (JWST) has the potential to do the same, detecting galaxies well out to $z \sim 12$ (Behroozi et al. 2020; Robertson 2022) due to its unparalleled NIR imaging and spectroscopic capabilities. The Near-InfraRed Camera (NIRCam) and the Mid-InfraRed Instrument (MIRI) on JWST are designed for broadband photometry from 0.7–25.5 microns with unprecedented resolution and sensitivity. Accepted Early Release Science (ERS), Guaranteed Time Observations (GTO), and General Observer (GO) programs

will carry out the first observations with JWST, test each instrument's capabilities, and set the tone for future science with Cycle 1 and beyond. These will allow us to extend observations of the galaxy rest-frame UV luminosity function to higher redshifts ($z > 10$) and fainter luminosity as well as detect rest-frame optical and NIR spectral energy distributions (SEDs) of high-redshift galaxies. Even with these amazing capabilities, spectroscopy of a large number of sources with JWST is unfeasible due to its short operational lifespan, and as MIRI has the smallest field of view of all the imaging instruments, we will obtain mid-IR data for less than a third of the survey area of our largest upcoming programs. As a result, most of the early surveys will carry out broadband imaging spanning ∼0.9–4.4 microns, with the NIR observations being instrumental for characterizing the rest-frame optical of z ∼7 galaxies, similar to what was done with Spitzer/IRAC photometry (e.g., Labbé et al. 2013; Oesch et al. 2014; Smit et al. 2015; Roberts-Borsani et al. 2016; Castellano et al. 2017).

For this reason, it is incumbent that we come up with an efficient and accurate method to select galaxies based on photometric colors alone, a method that retains its efficiency and accuracy in the JWST era. The most widely used method for $z \leqslant 4$ galaxies is the *UVJ* diagram. Star-forming and quiescent galaxies have been shown to exhibit a bimodality in the rest-frame $U - V$ versus $V - J$ color–color space out to $z \sim 3$ (Labbé et al. 2005; Williams et al. 2009; Whitaker et al. 2011; Muzzin et al. 2013; Straatman et al. 2014, 2016). This bimodality correlates with specific star formation rate (SFR), MIPS 24 micron flux down to implied SFRs of ∼40 $M_{\odot}yr^{-1}$ (Brammer et al. 2011), and morphology (Papovich et al. 2012; Patel et al. 2012; Papovich et al. 2015). Additionally, dusty star-forming and quiescent galaxies are difficult to distinguish in single-color diagrams (e.g., *U*–*V* alone; Brammer et al. 2009; Wolf et al. 2009; Leja et al. 2019b), as both SED types exhibit red colors and peak at 1 μm in the rest frame. The physical motivation then for including a second color (e.g., *V*–*J*) is to add a longer wavelength baseline in order to trace out the rest-frame NIR, where dusty star-forming galaxies tend to have redder colors, and quiescent galaxies have bluer colors. Consequently, the *UVJ* diagram is a useful and efficient way of selecting different galaxy populations in large photometric data sets.

Despite its utility, the *UVJ* diagram is fraught with problems at $z > 3$. Due to the growing number of spectroscopically confirmed quiescent samples at these redshifts, we now know that *UVJ*-selected quiescent samples have 21%–30% contamination from galaxies with significant levels of ongoing star formation (e.g., Schreiber et al. 2018; Forrest et al. 2020a). There are several reasons for this. One is that the Hβ+[O III] lines can boost the *V*-band flux, causing galaxies with strong emission lines to appear redder in $U - V$ than they actually are. Additionally, *J*-band fluxes at $z > 3$ are less accurate because they require extrapolation. This occurs because the *J* band corresponds to the Spitzer/IRAC bands at these redshifts, for which the data is often shallow (typically by ≃2.5 mag, if it is available at all; Sanders et al. 2007; Ashby et al. 2015).

In this paper, we present a new set of synthetic top-hat filters to better separate galaxies in different stages (quiescent versus star-forming) using $(g_s - i_s)$ versus $(u_s - g_s)$ colors (a $(ugi)_s$ diagram). The outline for this paper is as follows. In Section 2, we describe the data sets we use to test the color-selection methods. In Section 3, we introduce the filters (u_s, g_s, and i_s), which lie at at 2900 Å, 4500 Å, and 7500 Å, respectively, and were designed to address the aforementioned issues for use with current ground-based photometric catalogs and in the JWST era (Figure 1). In Section 4, we highlight the necessity for a new set of filters for use at $z > 3$ by demonstrating the effects of extrapolation on *UVJ*. Finally, we evaluate the sample selection efficiency and limitations of each method in Section 5. Throughout, we assume a ΛCDM cosmology with $\Omega_M = 0.3$, $\Omega_\Lambda = 0.7$, and $H_0 = 70$ km s^{-1} Mpc^{-1}. Rest-frame colors are quoted in AB magnitudes (Oke & Gunn 1983), and stellar population parameters were computed using a Chabrier initial mass function (Chabrier 2003).

2. Data and Methods

2.1. Observational Data (0.5 < z < 4)

To test and calibrate the color–color methods, we employ four galaxy catalogs that provide both observed and rest-frame colors (we derive these ourselves where not provided), high-quality measures of photometric (or spectroscopic) redshifts, stellar masses, and SFRs. These are important as we wish to test the ability of selection methods to identify galaxies in active and quiescent stages of their evolution. We therefore opt to employ both theoretical catalogs constructed from known details about stellar population models (Section 2.2) and real catalogs that contain physical high-redshift galaxies with imperfect knowledge of their stellar populations, dust attenuation, and emission-line contributions (Sections 2.1.1 and 2.1.2). It is important to understand color–color selection efficacy from both types of catalogs as we move into the even more distant universe.

2.1.1. 3D-HST

Some of the empirical catalogs we use are those from 3D-HST (Skelton et al. 2014), as these provide some of the most robust results from SED fitting, but are limited to $z < 2.5$ (because the catalogs are selected in the HST/F160W band). The data were taken in five well-studied extragalactic fields of CANDELS (Grogin et al. 2011; Koekemoer et al. 2011) imaged in 19–45 photometric bands. We use the results of `Prospector` fits to the 3D-HST photometric catalogs from Leja et al. (2019c). The 3D-HST catalogs provide observed-frame 0.3–24 μm photometry and redshifts for ∼200,000 galaxies, complete down to $10^9 M_{\odot}$ at $z = 2$ (Tal et al. 2014). The catalog redshifts comprise, in order of accuracy, (1) ground-based spectroscopic redshifts, (2) NIR grism redshifts (Momcheva et al. 2016), and (3) photometric redshifts from `EAZY` (Brammer et al. 2008).

We use stellar population parameters inferred with the 14-parameter Bayesian SED-fitting `Prospector-`α framework described in Johnson & Leja (2017), Leja et al. (2017), fit to a 90% stellar mass-complete sample of 58,461 of galaxies at $0.5 < z < 2.5$ (Leja et al. 2019c). The lower-redshift limit ($z = 0.5$) is set by the redshift at which the aperture photometry starts to become unreliable. `Prospector-`α utilizes the wide variety of physical implementations available in `FSPS` (Conroy & Gunn 2010), including a flexible six-parameter nonparametric star formation history (SFH), state-of-the-art MIST stellar isochrones, a wide range of stellar metallicities, a two-component dust attenuation model with a flexible dust attenuation curve, dust emission via energy balance, nebular line and continuum emission, and a model for the mid-infrared emission of dusty active galactic nucleus (AGN) tori. All of these enable `Prospector-`α to mitigate the persistent factor

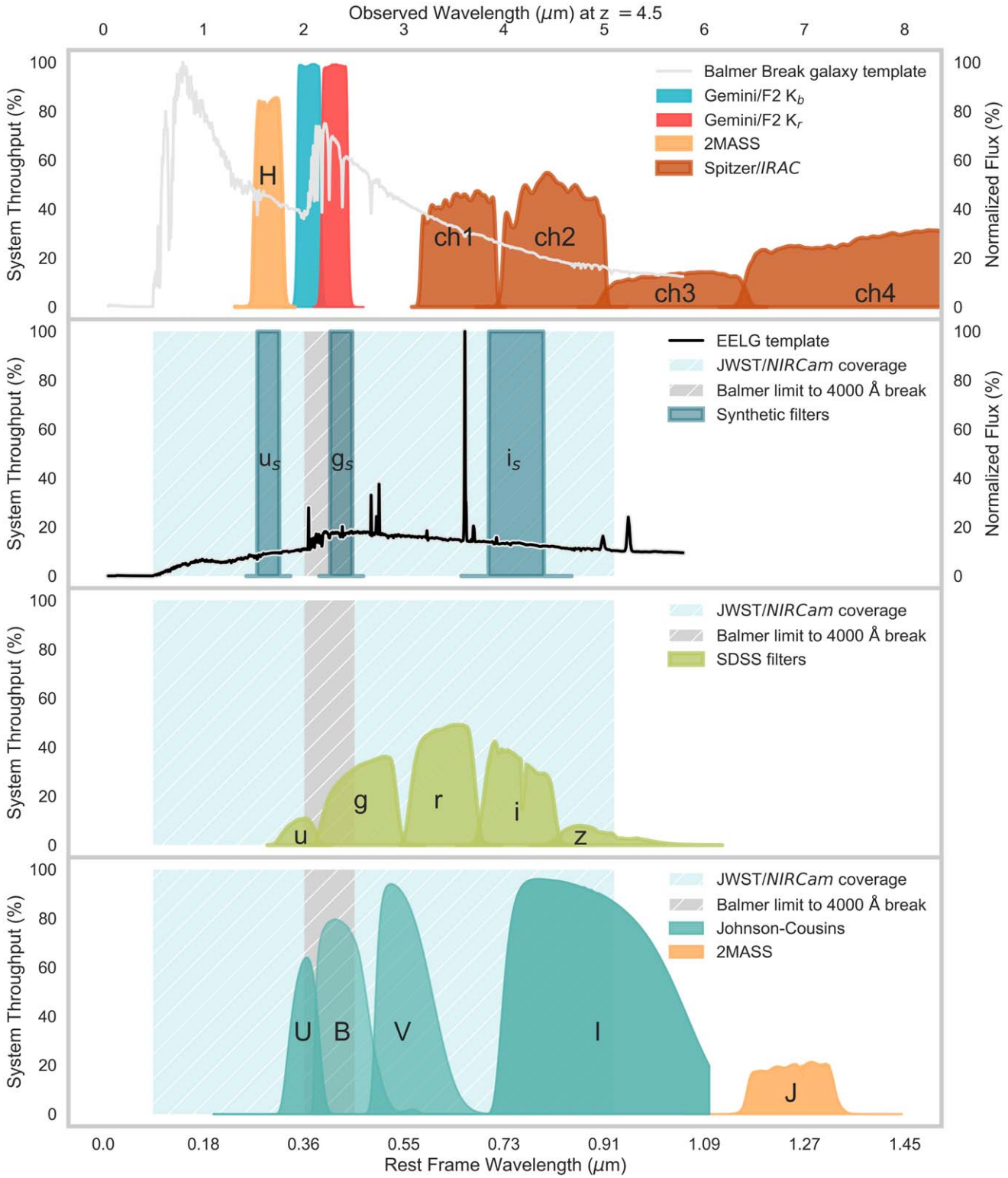

Figure 1. *Classic* photometric bands available in extragalactic catalogs and rest-frame color schemes. Rest-frame *UVJ* colors at $z > 3$ require extrapolation because the *J* band is redward of 5 μm (and it overlaps with Spitzer/IRAC channels 3 and 4, for which there is often limited or no data). This will be a problem even with JWST/NIRCam observations, because they will also only extend out to 5 μm. Additionally, the *V*-band band will be susceptible to artificial boosting from galaxies with strong Hβ+[O III] emission lines (at 0.49–0.51 μm, illustrated by the SED of the extreme-emission-line galaxy in the second panel), which comprise a significant fraction of star-forming galaxies at $z > 3$, reaching ~50% by $z = 6$. We introduce a set of synthetic $(ugi)_s$ filters (second panel) designed to mitigate these problems by (1) being more sensitive to the 4000 Å/Balmer break; (2) avoiding common emission lines; and (3) maintaining overlap with the Spitzer/IRAC and JWST/NIRCam filters out to $z = 6$.

of 2 uncertainty in stellar masses and SFRs derived by SED-fitting codes (Papovich et al. 2001; Marchesini et al. 2009; Muzzin et al. 2009; Wuyts et al. 2009; Behroozi et al. 2010; Pforr et al. 2012; Conroy 2013; Mitchell et al. 2013; Leja et al. 2015; Mobasher et al. 2015; Santini et al. 2015; Tomczak et al. 2016; Carnall et al. 2018; Leja et al. 2019c) by making it

possible to model systematics on stellar masses and SFRs galaxy by galaxy.

We note that, although $UV + IR$ SFRs, which are intended to be more reliable than those from SED-fitting codes, as they account for reprocessed emission from dust-obscured star formation, are available for the 3D-HST catalogs (e.g., Whitaker et al. 2014; Barro et al. 2019), they tend to underestimate the flux from old ($t > 100$ Myr) stellar populations. This becomes particularly important for low sSFR objects, with the UV and IR luminosity from old stars comprising $\sim$50% of the total flux at log (sSFR < -10.5), and dominating the total light output at log (sSFR $= -13$) (Leja et al. 2019c; Martis et al. 2019). Because our study is primarily concerned with selecting highly pure samples of quiescent galaxies (which generally have low sSFRs), we chose the SFRs inferred by this modified Prospector-α model, which self-consistently estimates the effect of dust heating by old stars, over catalogs based on $UV + IR$-derived SFRs.

Additionally, we compare our findings with Prospector-α to those using SFRs, stellar masses, and dust extinction from FAST (Kriek et al. 2009; provided with the 3D-HST catalogs) because this has been the traditional choice in the literature. These are based on single-parameter, τ-model SFHs, where the SFR scales as $\exp(-t/\tau)$ (for an e-folding timescale, τ). Although FAST stellar masses are well constrained because they mostly depend on rest-frame optical photometry, which is well covered by the 3D-HST data, SFRs and dust are not (Wuyts et al. 2012). We discuss this further in Section 5.1. In this work, we use a subsample of galaxies with reasonable photometry (i.e., 3D-HST use_phot =1, with K_s signal-to-noise ratio, hereafter S/N, $\geqslant$7) and stellar mass $M_* > 10^{10}\,M_\odot$. The reported SFRs from Prospector-α are averaged over the most recent 100 Myr (rather than instantaneous values).

2.1.2. UltraVISTA

Catalogs such as CANDELS and 3D-HST lack large samples of galaxies at the upper end of the stellar mass function, particularly at the highest redshifts (e.g., Merlin et al. 2018) because they have a small survey area ($\sim$0.2 deg^2). Old and dusty galaxies tend to be better sampled by K-selected surveys. For this reason, we also use results from the UltraVISTA survey (McCracken et al. 2012), which covers 1.5 deg^2 in the COSMOS field with multiwavelength data, and better samples massive galaxies at high redshifts. For galaxies at $2.5 < z < 4$, we use MAGPHYS fits from Martis et al. (2019) to the UltraVISTA DR3 catalog, which is mass-complete at $\log(M_*/M_\odot) > 10.5$ out to $z \simeq 4$. This deep catalog (5σ limiting magnitude in $K_s = 25.2$ mag) includes UV–NIR photometry spanning 49 bands. These were supplemented with Spitzer/MIPS 24 μm observations and 100 and 160 μm observations from the Herschel PACS Evolutionary Probe (Lutz et al. 2011), and 250, 350, and 500 μm observations from the Herschel Multi-Tiered Extragalactic Survey (Oliver et al. 2012). Redshifts in the catalog are either from the EAZY photometric redshift code or spectroscopic redshifts where available.

Martis et al. (2019) used the high-z extension of MAGPHYS (da Cunha et al. 2008; Cunha et al. 2015) to model the UV–FIR photometry of the UltraVISTA sources. The SFH is parameterized as a continuous delayed exponential of the form $\gamma^2 te^{(-\gamma t)}$, where γ is the inverse of the star formation timescale, τ. This form allows high-redshift galaxies to have SFHs that rise with time (negative t), suggested by many observations at high redshifts (Lee et al. 2010; Papovich et al. 2011; Reddy et al. 2012; Carnall et al. 2019). Additionally, it helps reduce systematic effects introduced by too simplistic functional forms of the SFH (e.g., exponentially declining; see Section 2.3). Moreover, the inclusion of the far-IR data from Herschel ensures stronger constraints on the estimated SFRs compared to those estimated from modeling the UV-to-NIR photometry alone. MAGPHYS SFRs are reported by averaging the most recent SFH over a 10 Myr period. For our sample, we select galaxies with K_s mag $\leqslant$ 23.5 AB.

2.2. Simulation Data at $4 < z < 6$

Our goal is to develop a simple color–color selection method for distinguishing samples of quiescent and star-forming galaxies that works well for current ground- and space-based photometric data, and also in the JWST era. To achieve this, we use the JWST extragalactic mock catalog, publicly available as the JWST Advanced Deep Extragalactic Survey (JADES) extraGalactic Ultradeep Artificial Realizations (JAGUAR) package (Williams et al. 2018). Unlike semianalytic models and hydrodynamical simulations, JAGUAR uses an empirically driven approach: modeling observed galaxy distributions and scaling relations and matching realizations to our deepest extragalactic surveys.

The JAGUAR catalog is briefly described as follows: number counts for star-forming and quiescent galaxies are determined using the Tomczak et al. (2014) mass functions and UV luminosity functions at $0 < z < 10$ (Bouwens et al. 2015; Oesch et al. 2018; for star-forming galaxies at $z > 4$). UV luminosity functions are used to estimate star-forming galaxy counts at $z > 4$, rather than stellar mass functions because the Balmer/4000 Å break shifts into NIR at these redshifts, where most facilities have low sensitivity, which could make stellar mass estimates at these redshifts uncertain. The downside to using UV luminosity functions, however, is that dusty star-forming galaxies, which are the primary contaminants of quiescent galaxies in color-selected samples, are underrepresented in UV-selected samples. We artificially infuse dusty star-forming galaxies into the JAGUAR catalog by reddening a subsample of star-forming galaxies using the Calzetti et al. (2000) dust law and the mass-dependent Pannella et al. (2009) relation for the extinction of star-forming galaxies in the ultraviolet (see Appendix A). Even with this addition, we see a dearth of dusty star-forming galaxies in the JAGUAR color–color plots (discussed further in Section 5.1.2).

JAGUAR generates mock SEDs and stellar population parameters for each galaxy using BEAGLE (Chevallard & Charlot 2016) and matches them to 3D-HST objects based on redshift and stellar mass (for $\log(M_*/M_\odot) > 8.7 + 0.4z$, which corresponds to $\log(M_*/M_\odot) = 9.89$, at $z = 3$). Outside the parameter space covered by 3D-HST, they adopt the properties of the mock SEDs from BEAGLE. To derive stellar population parameters, they use a delayed exponential SFH and model stellar emission with the Bruzual & Charlot (2003) stellar population synthesis code. The JAGUAR catalogs incorporate line and continuum emission from gas photoionized by young, massive stars using the Gutkin et al. (2016) models and dust attenuation by the two-component model of Charlot & Fall (2000). The catalog contains broadband photometry in HST and JWST/NIRCam filters from 0.4–4.8 μm, emission-line measurements, and galaxy morphological properties. As with

the data sets above, we use JAGUAR SFRs averaged over the most recent 100 Myr.

2.3. Rest-frame Colors

Using the aforementioned data sets (3D-HST, UltraVISTA, and JAGUAR), we derive $(ugi)_s$ rest-frame colors using `eazy-py` (Brammer 2021), a Python-based SED-fitting code based on the photometric redshift fitting code `EAZY` (Brammer et al. 2008). `EAZY` was built to handle the faint galaxy samples with limited spectroscopic redshifts, as we often have with deep NIR photometric surveys. It fits a nonnegative, linear combination of empirically derived templates (in a user-defined list) to the observed photometry. Two features that distinguish `EAZY` from other photometric redshift fitting codes and make it ideal for fitting high-redshift galaxies are (1) a template error function, which seeks to account for wavelength-dependent corrections of the templates, such as variations in the dust extinction law and missing spectral features; and (2) an apparent magnitude prior, which assigns low probabilities to low-redshift solutions for extremely bright galaxies at high redshift.

One of the important modifications `eazy-py` makes to `EAZY` is that it determines rest-frame colors by doing a *weighted interpolation*. It refits the templates to the data, weighting more strongly the observed photometry that is nearest the rest-frame band (in wavelength) and down-weights photometry that is farther away. The rest-frame colors are then interpolated from the model fluxes flanking the rest-frame band of interest.

Generally, the way the best-fit SED is determined impacts the derived rest-frame colors. When the best fit is an arbitrary linear combination of templates (as it is in `EAZY` and `eazy-py`), this method produces similar results as interpolating from the observed photometry. This is important to note, as rest-frame colors that are based on the best-fit SED are heavily influenced by the choice of template set and the assumed SFH. Merlin et al. (2018) found that rest-frame *UVJ* colors can differ by up to 0.3 mag when using an exponentially declining (τ) SFH versus a top-hat SFH, and this change occurs mostly in the $V-J$ direction. Rest-frame colors based on the observed photometry are not subject to these systematics; however they are more sensitive to sharp effects (e.g., emission lines and spectral breaks) and low S/N. `eazy-py` adopts the best features of each method by using empirical template sets (which do not assume SFH) and using all the available photometry, weighting more strongly bands closest to the rest-frame band of interest. This way, the estimated uncertainties on the rest-frame colors (e.g., Figures 5, 6, and 7) are purely statistical and not prone to the limitations and biases of the chosen template set and SFH (we return to this issue in Section 5.3.2).

For catalogs that provide *UVJ* and *ugi* colors, we use those, as they are tied to the stellar masses and SFRs, that we use for the subsequent analysis in this paper. This applies for instance to the *UVJ* colors from `Prospector-`α from $0.5<z<2.5$ (Figure 3), which were determined by marginalizing over the likelihoods of the SED parameters. For catalogs that do not provide rest-frame colors (e.g., JAGUAR), we use a set of 10 templates that model the following galaxy populations: emission-line galaxies, galaxies that that are both old and dusty, old quiescent galaxies, and post-starbursts. These templates are the same as those employed in the 3D-HST and UltraVISTA surveys. We used the v.1.0. template error function and fixed the redshifts to the provided photometric (or spectroscopic redshifts).

Table 1
Synthetic Filter Details

Filter Name	λ_c (Å)	$\Delta\lambda$ (Å)
Synthetic u (u_s)	2900	400
Synthetic g (g_s)	4500	400
Synthetic i (i_s)	7500	1000

Note. Central wavelengths (λ_c) and widths ($\Delta\lambda$) of our proposed $(ugi)_s$ filters.

Finally, we tested the robustness of our rest-frame $(ugi)_s$ colors when derived using broadband JWST photometry. This is important to consider because unlike preexisting photometric catalogs, which have data in 25+ photometric bands (Sections 2.1.1 and 2.1.2), those from ongoing Cycle 1 programs in extragalactic fields with little-to-no ancillary data will have photometry in ∼10 JWST/NIRCAM bands. The JAGUAR catalogs provide simulated broadband HST/ACS (Advanced Camera for Surveys) and JWST/NIRCAM photometry for the JADES GTO program. This allows us to obtain realistic estimates of the uncertainties on rest-frame fluxes derived using JWST catalogs at $2<z<6$. We find that the median fractional uncertainty (σ_f/f) for rest-frame fluxes derived using broadband JWST/NIRCAM photometry is <21% for the synthetic i (i_s) and SDSS i bands and <50% for 2MASS J. Including medium-band photometry improves these uncertainties by ∼10%.

3. Filter Design and Calibration

3.1. The Ideal Filter Combination

The ideal filter set for distinguishing star-forming galaxies from quiescent galaxies at $z>3$ should match *UVJ* in simplicity and convenience while reducing the biases inherent in *UVJ* selection such that it will be useful even in the JWST era. We designed a set of top-hat filters with central wavelengths at 2900 Å, 4500 Å, and 7500 Å (Table 1), corresponding to the SDSS u, g, and i filters, respectively, shown in Figure 1.

The synthetic filters were designed to accomplish three main goals. First, they robustly straddle the Balmer/4000 Å break, similar to the synthetic U_m and B_m filters in Kriek et al. (2010). The wider wavelength spacing of the u_s and g_s filters combined with their narrower widths means that the Balmer break produces a stronger color signature in u_s-g_s than in $u-g$ and $U-V$. We see this in the color evolution of stellar population tracks in each diagram (Figure 2), with the $\tau=100\,Myr$ model entering the quiescent region ∼250 and ∼150 Myr earlier in $(ugi)_s$ than those in *UVJ* and *ugi*, respectively. We explore this idea further in Section 5.3.1. For this reason, the $(ugi)_s$ filters complement data from NIR medium-band surveys, which were designed to achieve higher-resolution sampling of the Balmer/4000 Å break. This includes new imaging using K_b and K_r filters ($R\sim10$) from the FENIKS survey, which split the K_s band into a bluer and redder filter, similar to the strategy employed by the NMBS and ZFOURGE surveys, which split the J and H bands for increased wavelength sampling of the Balmer break. These K_b and K_r filters have been shown to

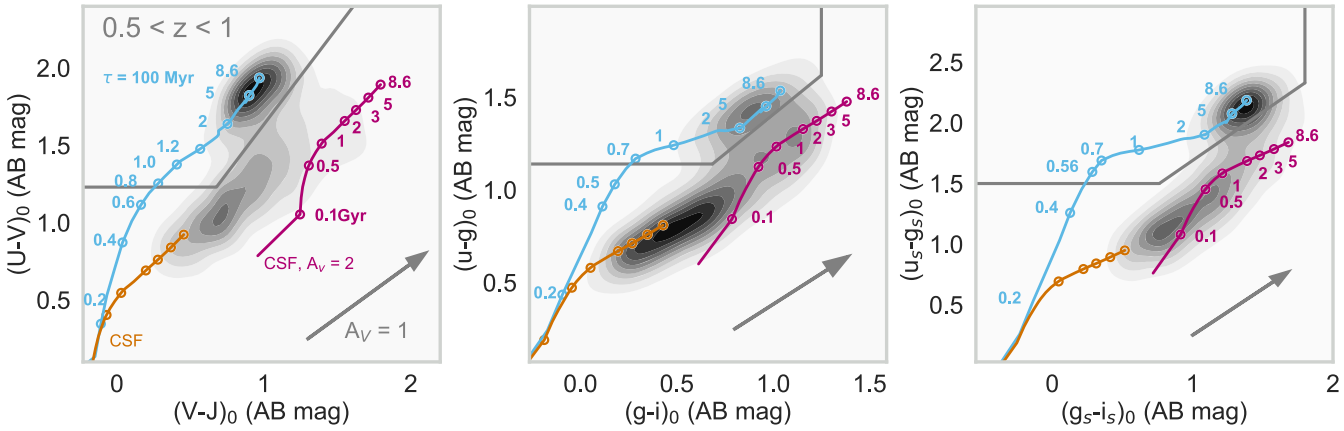

Figure 2. Color evolution tracks of 10^{11} $M_{\odot}$ FSPS models with various star formation histories at metallicity = 0.5 $Z_{\odot}$: an exponentially declining SFH with e-folding timescale $\tau = 100$ Myr (blue), a constant SFH with no dust (CSF, orange), and $A_v = 2$ (magenta) in *UVJ* (left), *ugi* (middle), and $(ugi)_s$ (right). Empty circles denote stellar population ages in Gyr for the lower-redshift boundary ($z = 0.5$). The contours show galaxies in 3D-HST at $0.5 < z < 1$. The gray vectors indicate 1 mag of extinction assuming a Calzetti et al. (2000) curve. The $\tau = 100$ *Myr* stellar population track evolves into the quiescent region ~250 and 150 Myr younger in $(ugi)_s$ than in *UVJ* and *ugi*, respectively. This suggests that $(ugi)_s$ captures recently quenched galaxies at younger ages than the other two color-selection methods.

reduce photometric redshift uncertainties by factors of 2 and 4 at $z < 3$, and $z > 4$, respectively, and reduce contamination from low-redshift interlopers, usually dusty star-forming galaxies, by a factor of 2 at $4 \lesssim z \lesssim 5$ (Esdaile et al. 2021). We plan to apply our $(ugi)_s$ selection to data from FENIKS in a forthcoming paper.

Second, the synthetic $(ugi)_s$ filters avoid regions with strong emission lines. These can boost photometry in a particular bandpass, mimicking red $U - V$ or blue $V - J$ colors, hence quiescence (Section 5.2). A similar problem occurs with SDSS $u - g$ colors. We can quantify the magnitude increase (Δm) in a filter of width $\Delta\lambda$ using the following, where W_0 is the equivalent width (EW) of the emission line (Papovich et al. 2001):

$$\Delta m \approx -2.5 \log\left[1 + \frac{W_0(1+z)}{\Delta\lambda}\right]. \quad (1)$$

A star-forming galaxy at $z = 3$, for instance, with a rest-frame Hβ+[O III] emission-line EW of 500 Å will boost the $U - V$ color by ≃1.2 mag. This problem is exacerbated at higher redshifts, because high EW objects comprise an increasingly larger fraction of the star-forming population in those regimes (Endsley et al. 2021; Tang et al. 2021). The synthetic filters solve this problem by avoiding [O II] (3727 Å), Hβ+[O III] (in the region 4863–5007 Å), and Hα+[N II] (in the region 6548–6563 Å). However the FWHM of the $(ugi)_s$ filters is small (400 Å compared to 991 Å for V and 1390 Å for SDSS g). This means that, although g_s should not be contaminated, if it is (e.g., due to photometric redshift uncertainties), a stronger magnitude change is introduced. We discuss this further in Section 5.3.2.

Third, the synthetic $(ugi)_s$ filters improve on uncertainties from the age–dust degeneracy while avoiding extrapolation. Galaxies with blue $U - V$ colors generally exhibit unobscured star formation. Those that are red in $U - V$, however, could be either galaxies that have evolved stellar populations or star-forming galaxies that are obscured by dust. However, because quiescent galaxies generally have relatively lower dust attenuation, they tend to have bluer $V - J$ colors. Thus, the longer the wavelength baseline, the higher the sensitivity to dust. It is for this reason that far-UV (FUV) and mid-infrared colors are more efficient than *UVJ* at selecting galaxies with low sSFRs (Leja et al. 2019b).

Unfortunately though, a longer wavelength baseline is more likely to require the extrapolation of observed-frame colors beyond where there is data in order to determine rest-frame colors. At $z \gtrsim 4$, the rest-frame J band corresponds to $\gtrsim$6 μm observed, generally only available from IRAC 5.8 μm and redder bands (e.g., forthcoming JWST/MIRI data). At longer wavelengths, the flux sensitivity of the IRAC data is substantially lower (by factors of 4 and 8 in IRAC channels 3 and 4 compared to IRAC channels 1 and 2); hence those data are often unavailable or too shallow (Figure 4).[15] Rest-frame *UVJ* colors at $z > 4$ therefore require extrapolation and hence are less reliable. Figures 5 and 6 illustrate the effects of extrapolation on the J band. The new synthetic filters proposed here cover the longest wavelength baseline that is possible while maintaining overlap with Spitzer/IRAC channels 1 and 2 and JWST/NIRCam coverage, to avoid extrapolation at redshifts out to $z \sim 6$ (the end of the epoch of reionization). We demonstrate the effects of extrapolation on colors using the rest-frame J band further in Section 4.

Finally, we discuss the choice of a synthetic u_s filter over an ultraviolet one (e.g., rest-frame *NUV*). $NUV - r$ or $FUV - V$ color selection, for instance, is a better discriminator of current versus past star formation activity than that of $U - V$ (Arnouts et al. 2007; Martin et al. 2007; Ilbert et al. 2010, 2013; Man et al. 2016; Leja et al. 2019b; Hwang et al. 2021). Similarly, the $FUV - V$ color has also been shown to have a much stronger correlation with specific SFR (Leja et al. 2019b). NUVrJ-selected quiescent samples have also been shown to have low contamination (⩽10%–15%) from dusty star-forming galaxies at $z \leqslant 3$ (Man et al. 2016; Hwang et al. 2021). These are all reasons to choose an ultraviolet filter over an optical u filter.

However, a rest-frame color selection involving a UV filter would miss recently quenched or *post-starburst* galaxies, particularly at high redshifts. Post-starbursts have intermediate-age stellar populations, which means that while they have strong Balmer/4000 Å breaks, they also have a higher UV continuum than that of a typical quenched galaxy due to residual star formation (see the template in the first panel of

[15] IRAC instrument handbook: https://doi.org/10.26131/irsa486.

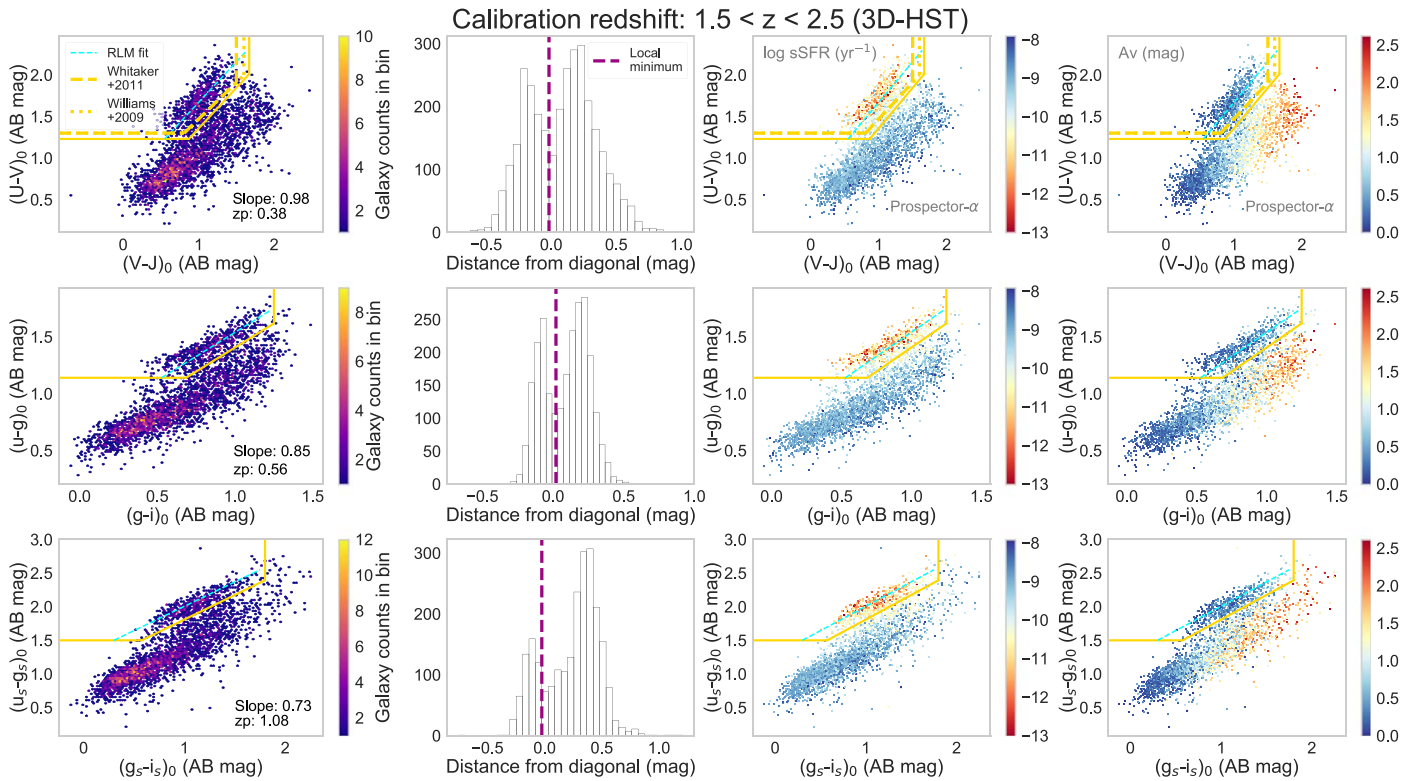

Figure 3. Calibration and validation of color–color diagrams. From top to bottom, the rows show different color–color schema applied to samples of galaxies from the 3D-HST catalog with stellar mass, $\log(M_*/M_\odot) \gtrsim 10$, and redshift range $z = 1.5$–2.5. Top: *UVJ*. Middle: *ugi*. And bottom: $(ugi)_s$. The left panel of each row shows the color–color distributions. We determine the slope of the diagonal line by fitting the *red sequence* (of galaxies in the upper left of each color–color space) using robust linear methods, which are less sensitive to outliers than ordinary least squares. We then measure the y-intercept (zero-point [zp]) by identifying a local minimum between the red and blue sequences (illustrated in the histogram in the second panel of each row). Similar to *UVJ*, the rest-frame *ugi* and synthetic $(ugi)_s$ colors correlate with specific star formation rate and dust estimates from `Prospector-`α, shown in the third and fourth panels in each row, respectively (dots show different galaxies color-coded by the aforementioned properties).

Figure 1). As a result of their elevated UV flux, their $NUV - r$ colors are *blue*, similar to those of star-forming galaxies. This has been demonstrated in the literature. For example, Valentino et al. (2020) showed two post-starburst galaxies at $z \sim 4$ that would be classified as star-forming using *NUVrJ*-selection and quiescent using *UVJ*.

By extension, post-starburst galaxies may be missed using rest-frame $NUV - g$ colors. These galaxies are observed (and expected) to be more common at higher redshifts ($z > 3$, e.g., Forrest et al. 2020b; D'Eugenio et al. 2020). It is therefore prudent to use a color-selection that will include them. For this reason, the rest-frame $u_s - g_s$ color is better suited to identify galaxies with colors typical of post-starburst galaxies, which will be an important class of objects at $z > 3$.

3.2. Color–Color Selection Criteria

In this section, we describe how we define the empirical *UVJ*, *ugi*, and $(ugi)_s$ selection criteria that separate quiescent and star-forming galaxies in our data. The basic quantities that we are interested in are the slope and y-intercept of the diagonal line, as well as the positions of the horizontal and vertical color cuts. These are based on a fit to an initial quiescent selection, which we vary until we obtain a clear bimodal distribution centered at zero. This process is a modification of the method in Kawinwanichakij et al. (2016). It is summarized as follows, and illustrated in Figure 3:

1. Find quiescent galaxies using literature criteria for the specified redshift where available (e.g., Williams et al. 2009; Whitaker et al. 2011; Muzzin et al. 2013 for *UVJ*) or by making an initial guess based on the distribution of data in color–color space (for *ugi* and $(ugi)_s$).
2. Update the slope of the diagonal line using the slope from iteratively reweighted robust linear methods (RLM) fit to a sigma-clipped subsample of the galaxies in the *red sequence* region of the color–color space (these are candidate quiescent galaxies). We opt to use RLM fits as they are less sensitive to outliers and do not assume homoscedastic errors (e.g., Croux & Rousseeuw 1992). This is illustrated in the first panel of each row of Figure 3.
3. Find the distance of each point in the data set from the diagonal line to delineate the red and blue sequences. This is illustrated in the second panel of each row of Figure 3.
4. Bin distances to determine the local minimum between the two sequences. The optimal number of bins is determined using the Freedman–Diaconis rule (Freedman & Diaconis 1981), which minimizes the area under the probability distribution function of the data and that of the function that best matches the data. Finally, we use the local minimum to update the y-intercept of the diagonal line.

We evaluate our method first by applying it to a sample of galaxies from the ZFOURGE survey (Straatman et al. 2016) and the third data release of the UltraVISTA survey at $0.3 < z < 1.6$, following Kawinwanichakij et al. (2016). Our

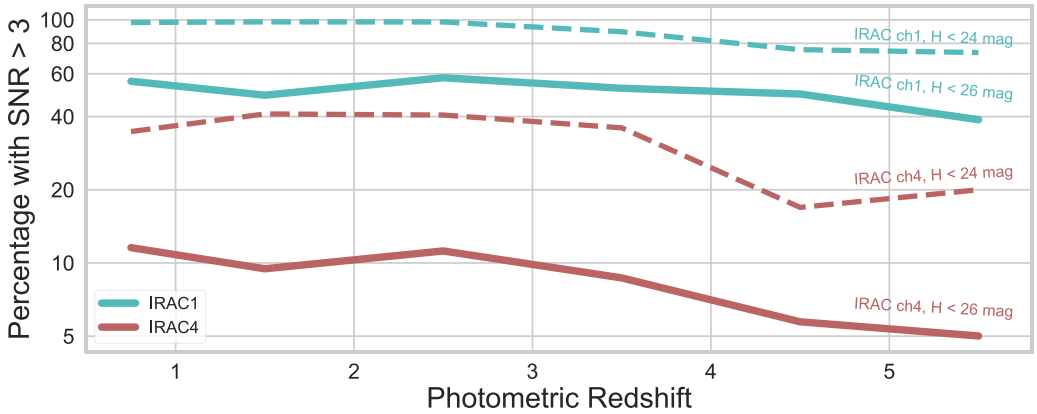

Figure 4. Percentage of detected galaxies with signal-to-noise ratio greater than 3 as a function of redshift for two of the reddest bands in our deepest photometric catalogs, Spitzer/IRAC channels 1 and 4 (with central wavelengths 3.6 and 7.9 μm). We use a sample of 32,528 galaxies in 3D-HST at $0.5 < z < 6$ with reasonable photometry and at two different detection limits (H mag < 24, and H mag < 26), with an additional requirement that the galaxy is detected in the K band (S/N > 5). Channels 1 and 4 correspond to the rest-frame J band at $z \sim 2$, and $z \sim 4.5$. This means that rest-frame UVJ colors will require extrapolation for up to ∼50% of galaxies at $z \sim 2$ and up to 95% of galaxies at $z \sim 4.5$. This problem will persist even with JWST data, as the NIRCam filter coverage does not extend beyond 5 μm, and MIRI data will be obtained for <30% of the survey area of upcoming GO, GTO, and ERS programs. The Spitzer/IRAC channels 2 and 3 data have similar detection fractions as channels 1 and 4, respectively.

zero-points and slopes for the aforementioned are within 0.02 and 0.17 mag of Kawinwanichakij et al. (2016) for the two data sets, respectively.

We then determine the color–color selection criteria for each data set used in this paper (3D-HST, UltraVISTA, and JAGUAR) using the method outlined above. This is important, as the color lines are not portable from one survey to another due to systematic biases (discussed further in Section 5.1). Because the observed data at $z > 3$ are sparse and generally of poorer quality, we calibrate the color–color lines on a broad redshift range ($z = 1.5$–2.5) and apply these calibrations to the entire data set, up to $z = 6$ in the discussion that follows. Calibrating the lines on a broad redshift range enables us to account for any evolution in the zero-point as a function of redshift. We apply a zero-point adjustment at $z = 4$–6 based on the UVJ colors of spectroscopic samples at $z = 3$–4 in the literature (Section 5.1.1).

Figure 3 shows a bimodality in each panel, indicating the presence of a distinct star-forming and quiescent population in all three color-selection methods: UVJ, ugi, and $(ugi)_s$. We define the selection of quiescent galaxies for each of the color–color selections in Figure 3 with the following criteria.

For UVJ,

$$(U - V) > 1.23 \ \wedge \ (V - J) < 1.67$$
$$\wedge (U - V) > (V - J) \times 0.98 + 0.38. \quad (2)$$

For ugi,

$$(u - g) > 1.14 \ \wedge \ (g - i) < 1.25$$
$$\wedge (u - g) > (g - i) \times 0.85 + 0.56. \quad (3)$$

For $(ugi)_s$,

$$(u_s - g_s) > 1.5 \ \wedge \ (g_s - i_s) < 1.8$$
$$\wedge (u_s - g_s) > (g_s - i_s) \times 0.73 + 1.08. \quad (4)$$

In all cases, $\wedge$ is the logical AND operator.

4. Effects of Extrapolation

UVJ colors at $z > 2.5$ can be uncertain because the rest-frame J band is subject to extrapolation. Generally, rest-frame colors are determined by interpolating between the two filters flanking the rest-frame band of interest (see Section 2.3 for a more detailed description). At $z = 3$, for instance, the J band overlaps with Spitzer/IRAC channels 1 and 2 at 3.6 and 4.5 μm, respectively. These data are often available (at S/N > 3) for only ∼55% of galaxies in our deepest photometric catalogs (Figure 4). This means that, for ∼45% of galaxies at $z \sim 3$, their rest-frame J fluxes are determined by extrapolating from the reddest observed data point. This problem is exacerbated at higher redshifts ($z \gtrsim 4$) because longer wavelength data (channels 3 and 4) are available for an even smaller fraction of galaxies (<7%).

The availability of mid-IR data with the JWST will not solve this problem. At the beginning of its mission, JWST will carry out a number of GO, GTO, and ERS surveys that are aimed at studying galaxies at high redshift. The largest programs (in order of decreasing survey area) are COSMOS-Web (Kartaltepe et al. 2021), Public Release IMaging for Extragalactic Research (PRIMER; Dunlop et al. 2021), JADES (Williams et al. 2018), and the Cosmic Evolution Early Release Science (CEERS; Finkelstein et al. 2017) survey. Together, these programs cover the five standard extragalactic fields (COSMOS, UDS, GOODS-N, GOODS-S, and EGS). Although they all include MIRI imaging, mid-IR data will be available for only a small portion of the surveyed area, due to the instrument's relatively small field of view. COSMOS-Web and PRIMER, which together survey COSMOS and UDS, will have MIRI coverage for up to ≃30% and ≃60% of their planned survey areas, respectively (noting that the survey area of PRIMER is only 1/6 that of COSMOS-Web). Additionally, the majority of planned MIRI observations will be shallow, i.e., 5σ depth $\lesssim$24 AB mag. For reference, the candidate $z = 5$ quiescent galaxy in Figure 5 has $m_{IRAC4} \approx 25$ AB mag. The latter two surveys, which cover GOODS-N, GOODS-S, and EGS, will have MIRI coverage for 7.4% and 25% of their total area, respectively. This means that we will have adequate MIRI coverage for only two out of the five extragalactic fields, and consequently a small fraction of galaxies surveyed. As such, extrapolation will continue to be a problem for the majority of galaxies at $z > 3$, even with JWST data.

We illustrate this with a candidate quiescent galaxy in the UltraVISTA catalog with a photometric redshift at $z_{ph} \simeq 5$

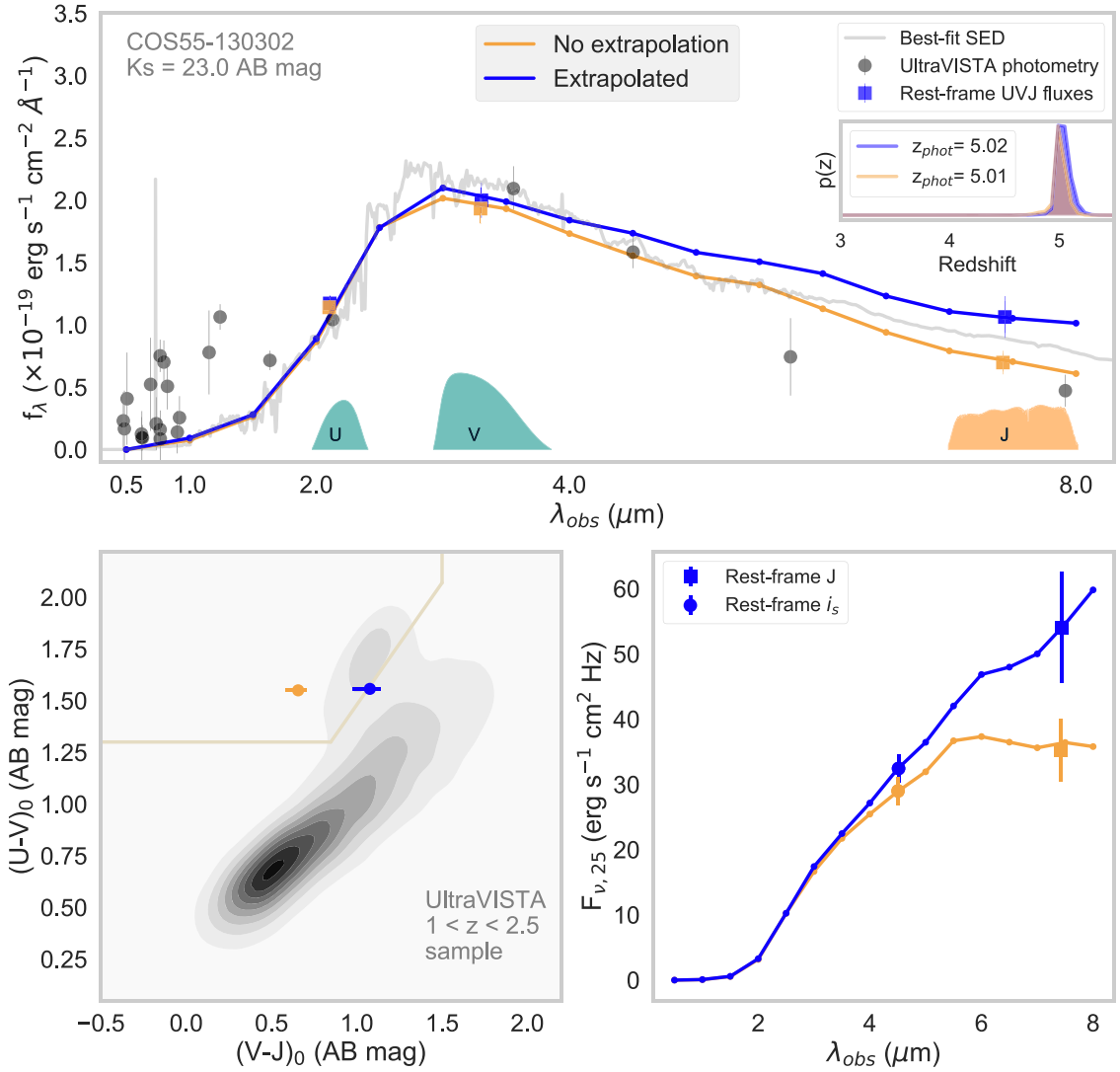

Figure 5. Examining the impact of extrapolation on the rest-frame *UVJ* colors of a $z = 5$ quiescent-galaxy candidate. Top: photometry, best-fit SED, and photometric redshift solution of COS55-130302 with extrapolation (blue curve/points) and without extrapolation (orange curve/points). For each case, we derive rest-frame fluxes in synthetic ($R = 10$) tophat filters in the observed frame (from 0.5 to 8 μm). We simulate extrapolation by removing the observed-frame photometry corresponding to the *J* band and redder. At $z = 5$, this corresponds to excluding data from Spitzer/IRAC channels 3 and 4, which is either unavailable or too shallow for at least 70% of galaxies at this redshift (Figure 4). Bottom left: although extrapolation has little impact on the best-fit SED and photometric redshift, it results in an almost factor of 2 difference in the estimated rest-frame *J*-band flux, resulting in a 0.46 mag change in $(V - J)_0$ color. Due to this extrapolation, galaxies like COS55-130302 can be erroneously scattered out of *UVJ*-selected samples. Bottom right: we repeat this experiment with the $(ugi)_s$ filters and find that our $(g_s - i_s)_0$ color, in comparison, is only affected by 0.08 mag, indicating that the $(ugi)_s$ diagram is better suited for selecting quiescent galaxies at $z > 4$.

(JWST GO Program #2362; Marsan et al. 2021). This galaxy offers an excellent example because it includes many high S/N photometric points from the UV to mid-IR, such that the true SED is well represented by the data. We simulate extrapolation by removing photometric points corresponding to the rest-frame *J* band (and redder) at that redshift. We then rederive the photometric redshift and rest-frame colors from the data using `eazy-py` (using the same method described in Section 2.3). We determine the rest-frame *UVJ* fluxes and corresponding uncertainties in the *nonextrapolated* case (where we use all available photometric bands) and the *extrapolated* case (where we have excluded bands corresponding to the rest-frame *J* band or redder, specifically IRAC channels 3 and 4 in this case). This latter case mimics the effects of extrapolation on the derived rest-frame *UVJ* fluxes, shown in Figure 5. We also show the rest-frame colors derived in synthetic top-hat ($R = 10$) filters spanning 0.5–8 μm for both cases.

Extrapolation (removing data points covering the rest-frame *J* band and redward) has a large impact on the derived rest-frame *J*-band flux (though it does not significantly change the redshift, which is constrained by the data near the Balmer/4000 Å break). In this case, the rest-frame *J*-band flux is changed by a factor of 2, causing the $V - J$ color to become redder by $\simeq$0.5 mag. This moves the galaxy out of the quiescent region of the *UVJ* diagram. We repeat this experiment with the $(ugi)_s$ filters (removing observed data corresponding to the i_s band and redder) and find that the $(g_s - i_s)_0$ color, in comparison, is only affected by 0.08 mag, indicating that the $(ugi)_s$ diagram is more robust against extrapolation and hence better suited to select quiescent galaxies at $z > 4$ with incomplete data.

Our findings with COS-130302 beg the question: how often do studies misclassify galaxies as quiescent using the *UVJ* diagram due to extrapolation? We investigate this by repeating

the experiment above on an S/N-limited sample (K_s S/N $\geqslant 5$) of galaxies at $0 < z < 6$ from the 3D-HST survey. This is illustrated in Figure 6. We quantify performance by measuring the normalized median absolute deviation ($\sigma_{\rm NMAD}$; Beers et al. 1990; Brammer et al. 2008) of the change in rest-frame colors ($\Delta(U-V)_0$ and $\Delta(V-J_0)$) of quiescent galaxies in the "non-extrapolated" (using all data) and "extrapolated" cases (removing any observed data corresponding to and redward of the rest-frame J band).

UVJ selection performs very well out to $z \sim 2$. For $z \lesssim 2$, the difference between nonextrapolated and extrapolated colors of quiescent galaxies is small, with $\sigma[\Delta(V-J)_0] \lesssim 0.1$ mag. At $z > 2$, the scatter increases to ∼0.3 mag, and it becomes much worse at $z > 4$, reaching $\sigma[\Delta(V-J_0)] \sim 1$ mag at $4 < z < 6$. $(U-V)_0$ colors also start to become extrapolated at $z \sim 2$, where the rest-frame V band enters the observed H band, which is only detected at S/N > 3 for up to ∼45% of galaxies at $z \gtrsim 2$ (estimated for Figure 4, not shown). This likely explains the factor of 2 increase in $\sigma_{\rm NMAD}$ (0.05–0.1) from $1 < z < 2$ to $2 < z < 3$ in $(U-V)_0$.

In contrast, the effects of extrapolation on the synthetic rest-frame $(ugi)_s$ colors are much lower, even at high redshift. Figure 7 shows the results. The change in $\Delta(ugi)_s$ colors remains small between the extrapolated and fiducial cases, with $\sigma[\Delta(ugi)_s] \leqslant 0.2$ mag at all redshifts, even at $4 < z < 6$.[16] Therefore, we conclude that extrapolation of the rest-frame J band can have a serious impact on the selection of quiescent-galaxy candidates at high redshifts ($z > 4$). This is especially important as the quiescent fraction is expected to decline sharply at this epoch (e.g., Merlin et al. 2019) such that these types of systematics of selection may dominate searches for such objects (see discussion in Section 5 below).

We note that these results are an illustration of the effects of extrapolation on the selection of high-redshift quiescent galaxies in the specific case where rest-frame colors are derived semiempirically. When they are estimated solely from the best-fit SED, as is typically done in the literature, the effects of extrapolation on a single galaxy are varied and dependent on many assumptions, including its intrinsic SED shape, S/N, redshift, the assumed SFH, and the template sets and parameters used for SED-fitting. Our experiments demonstrate the need for an updated color-selection method for high-redshift galaxies. This will continue to be necessary in the JWST era. We have demonstrated that the effects of extrapolation on our proposed synthetic $(ugi)_s$ filters will be minimal out to $z \sim 6$.

In the remaining sections, we show that the synthetic $(ugi)_s$ filters match *UVJ* in simplicity and discrimination efficiency, making $(ugi)_s$ a viable replacement.

5. Purity Tests and Discussion

5.1. Tests of Completeness and Contamination Using Color–Color Selection

Color-color selections involve a balance between sample purity and completeness. Generally, the higher the completeness, the higher the number of contaminants and vice versa. This tradeoff becomes increasingly important for quenched galaxies at higher redshift ($z > 3$), where features such as the Balmer/4000 Å break, which are key for determining photometric redshifts, are shifted into the NIR, a regime prone to numerous systematics. Additionally, the galaxies at those redshifts generally have lower signal-to-noise photometry, which can decrease the accuracy of rest-frame colors. As a result, dusty star-forming galaxies,[17] which are the primary contaminants of quiescent samples, are more likely to scatter into the quiescent region. Furthermore, the galaxies with strong nebular line emission (e.g., strong [O III] emission) are another source of contamination, and such sources comprise a greater fraction of the star-forming population at these redshifts (Endsley et al. 2021). Efficient color–color selection of galaxies at these redshifts therefore requires careful culling of such objects in order to maintain high completeness while lowering the contamination rate. In this section, we contrast the performance of the $(ugi)_s$ diagram with that of *ugi* and *UVJ* as it pertains to identifying and removing such interlopers.

One major challenge is evaluating *truth* in the purity and contamination of quiescent-galaxy searches. Several approaches have been taken in the literature, including using estimates of galaxy SFRs (and specific SFRs; e.g., Heinis et al. 2014; Chang et al. 2015; Tasca et al. 2015; Pacifici et al. 2016; Tomczak et al. 2016). Others identify active galaxies based on emission-line strength (e.g., Rodighiero et al. 2014; Belfiore et al. 2018) or far-IR emission (e.g., Whitaker et al. 2014; Ilbert et al. 2015; Lee et al. 2015; Schreiber et al. 2015; Erfanianfar et al. 2016). Speagle et al. (2014), Popesso et al. (2019) showed that the slope of the SFR–M^* plane, commonly referred to as the star-forming main sequence (SFMS), changes by up to 1 dex depending on which of these methods is used. Similar results were found with the Illustris-TNG simulations, with quiescent fractions on the higher-mass end ($\log(M_*/M_\odot) > 10.5$) varying between 20% and 40% (Donnari et al. 2019). Moreover, these thresholds only correspond to a *relative* quiescence because they fail to account for the evolution in the intrinsic stellar populations of quiescent galaxies over cosmic time, making them applicable only to a specific redshift or stellar mass bracket. Additionally, while *UV + IR* SFRs, which some regard as the *gold standard*, are available for our data set at $z < 4$, these can be problematic for a number of reasons. This is because IR luminosities (typically estimated from the 24 μm flux) tend to overestimate SFRs by up to a factor of 4, because they do not account for heating from intermediate age and old stars, which tends to dominate the IR budget for $\log(\mathrm{sSFR}) < -13$ (Belli et al. 2017; Fang et al. 2018; Leja et al. 2019c; Martis et al. 2019). Simulations also report similar findings, i.e., that UV luminosities can be overestimated by 0.2–0.5 dex at $z = 1$–4 for galaxies with $\log(M_*/M_\odot)$ ≈8.5–10.5 (Katsianis et al. 2020) and that the total IR luminosity is not a good proxy for dust-obscured star formation for rapidly quenched or "post-starburst" galaxies (Roebuck et al. 2019). In summary, the definition of what constitutes *truth* in quiescent-galaxy selection matters.

To mitigate this effect, we choose a data-driven approach. In order to determine which galaxies are truly quiescent, we take SFR and stellar mass estimates for galaxies from two catalogs that account for these systematics by self-consistently modeling

[16] The effects of extrapolation on $U-V$ color may be reduced with JWST/NIRCam data because, unlike with ground-based telescopes, a number of narrow, medium, and broadband filters exist between the K band and IRAC channel 1. Nevertheless, these effects will likely persist for $V-J$ colors.

[17] These can be either dusty galaxies *at the same redshift* as the quiescent galaxies or at lower redshift whose colors mimic those of high-redshift quiescent galaxies. Most of the dusty contaminants, however, will fall into the former category. The placement of the $(ugi)_s$ filters along the Balmer/4000 Å break will help reduce the effect of the latter (see Section 3).

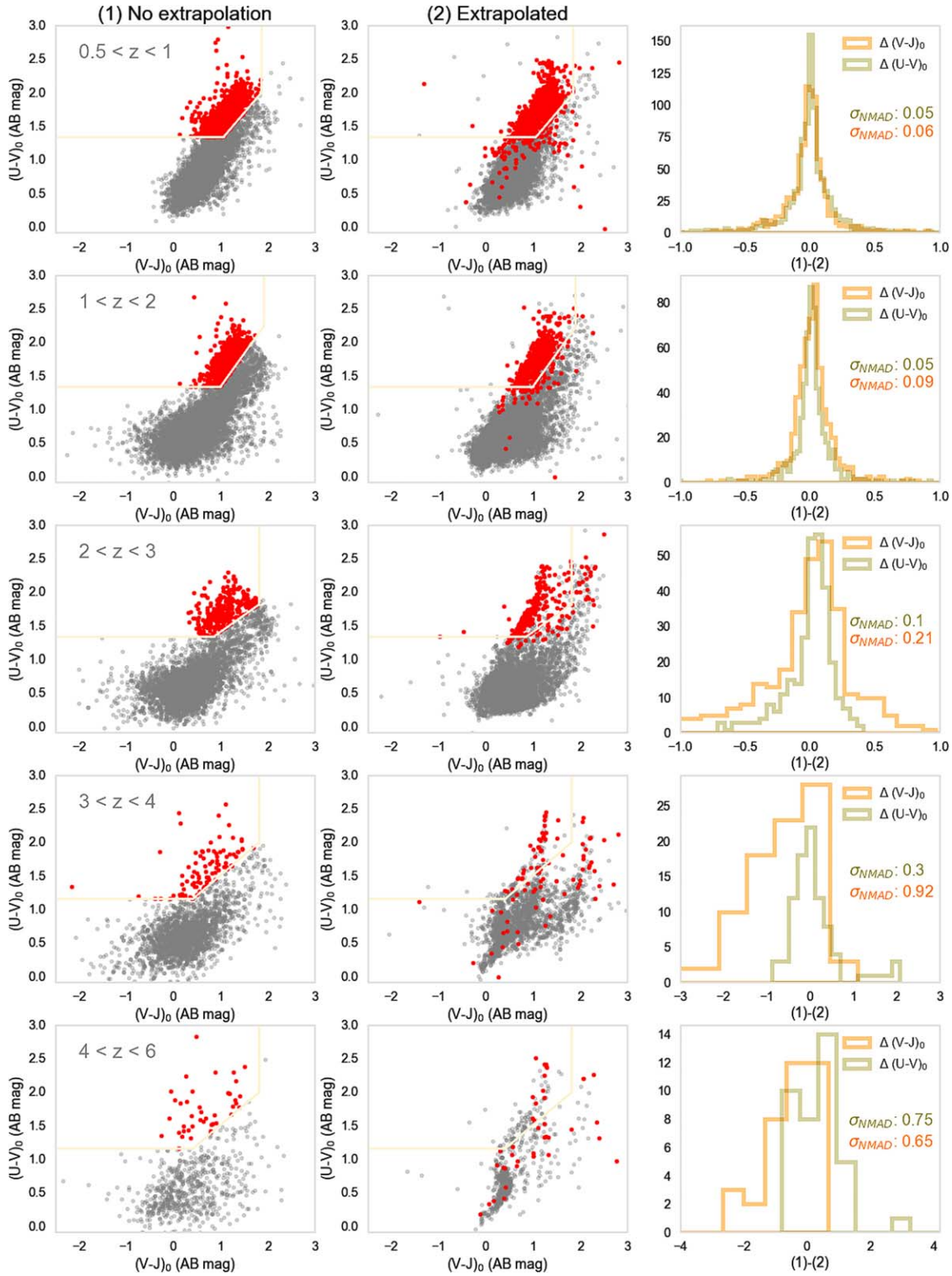

Figure 6. Impact of extrapolation on *UVJ*-selected quiescent galaxies with rest-frame *J*-band coverage from Spitzer at $0.5 < z < 6$. Each row shows the galaxies in bins of increasing redshift (top to bottom). The left panel in each row shows the distribution using rest-frame colors derived with all the available photometry (no extrapolation). The red dots show galaxies selected as *UVJ*-quiescent. The middle panel of each row shows the colors of the same galaxies on the left when the rest-frame colors are extrapolated (when the observed fluxes corresponding to the *J* band and redder are removed). The right panel of each row shows the distributions of the difference in $U - V$ and $V - J$ colors between the nonextrapolated and extrapolated cases for the quiescent galaxies. We quantify this change using the normalized median absolute deviation ($\sigma_{\rm NMAD}$). The effects of extrapolation are seen as an increase in $\sigma_{\rm NMAD}$ with increasing redshift, with $\sigma(\Delta[V - J])$ increasing from 0.2 mag at $z \sim 2$ to >0.65 mag at $z > 3$. NB: the abscissa ranges in the top three right-hand plots are the same; however we adjust it for the bottom two ($z > 3$) to better show the large change extrapolation introduces to rest-frame colors at these redshifts.

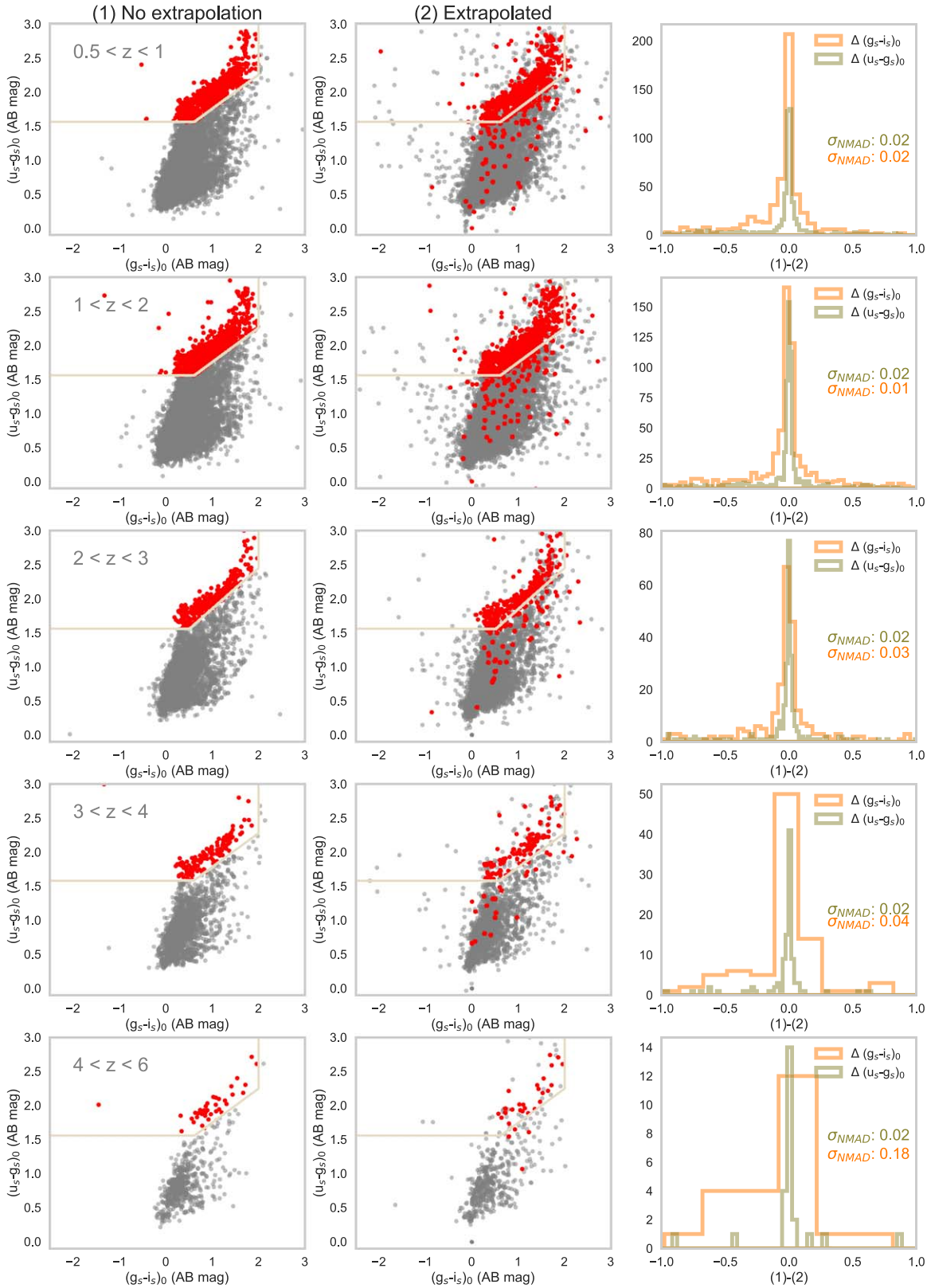

Figure 7. Similar to Figure 6, but showing the impact of extrapolation on synthetic $(ugi)_s$-selected quiescent galaxies at $0.5 < z < 6$. The $(ugi)_s$ filters are more resistant than that of *UVJ* to the effects of extrapolation, particularly at $z > 4$. The scatter in the distribution of the change in $(g_s - i_s)_0$ (right panels in each row) increases only slightly with redshift and is never higher than $\sigma(\Delta[g_s - i_s]) = 0.2$ mag. This is significantly improved compared to the effects of extrapolation on the *UVJ* colors. NB: the limits of the abscissa of the right-most panels are the same in all rows and the same as that of the first three rows of Figure 6.

the entire SED: the Leja et al. (2019c) measurements from `Prospector-`α for 3D-HST galaxies at $0.5 < z < 2.5$, and the Martis et al. (2019) measurements from `MAGPHYS` for galaxies in UltraVISTA at $z = 3-4$. Leja et al. (2019c) use Bayesian modeling methods with flexible SFHs that allow for more accurate estimates of galaxy SFRs (derived from

panchromatic data, i.e., UV − mid-IR). These estimates are appropriate for galaxies out to $z \lesssim 3$ as they are based on galaxies selected in the *H* band (and at higher redshifts, the Balmer/4000 Å break shifts beyond the HST/WFC3 *H*-band coverage). The catalogs of Martis et al. (2019) are based on UV − far-IR SED modeling using a rising SFH that accounts for stochasticity. For massive galaxies ($\log M_*/M_\odot > 10.5$), these provide useful constraints on distinguishing star-forming and quiescent galaxies at $z > 3$. Both catalogs include the effects of emission lines on the rest-frame colors, which allows us to also test contamination from sources with strong emission lines. We described these catalogs in detail in Section 2.

We then define regions in the specific SFR (sSFR)–stellar mass plane that separate star-forming galaxies from those that are quiescent. We identify a "ridgeline," i.e., the density peak in the SFR–mass plane, which corresponds to star-forming galaxies (Renzini & Peng 2015). At lower sSFRs lies the "green valley," below which lie the quiescent galaxies (Schawinski et al. 2014; Sherman et al. 2021). The advantage of this approach is that it does not depend on any preseparation of quiescent and star-forming galaxies, because the star–forming sequence is directly measured from the data.

We then divide the data into five redshift bins from $0.5 < z < 4$ and determine its 3D distribution by dividing the data into 0.3 dex square bins. In each redshift bin, we define the green valley by determining where the data fall below 10% of the star-forming density peak. In Figure 8, we show the two- and three-dimensional SFR-M* plane as well as the green valley, denoted by the white line. The mass range covered by the data reflects the 90% completeness limit at each redshift (taken from Skelton et al. 2014 for 3D-HST; and Martis et al. 2019; and Marsan et al. 2022 for UltraVISTA). *UVJ*-quiescent galaxies are shown in red. We define *true* quiescent galaxies as those with a sSFR below the estimated location of the *green valley* using the definition above.

5.1.1. Results at $z \leqslant 4$

In Figures 9 and 10, we contrast the performance of the $(ugi)_s$ diagram with those of *ugi* and *UVJ*. Figure 9 shows that our definition of quiescence correctly selects the galaxies with low sSFRs and low dust extinction (as a function of redshift), and that the majority of the contaminants are dusty galaxies with low sSFRs. In Figure 10, we quantify this performance, also showing results using *UVJ*-selection criteria from Williams et al. (2009), Whitaker et al. (2011). Completeness here is defined as the number of true positives (TP; galaxies with specific SFRs below the threshold of the green valley in Figure 8) in the quiescent region divided by the total number of TP in the sample. By this definition, the false negative fraction (i.e., the number of true quiescent galaxies missed) is 1−Completeness. The contamination rate is the number of selected false positives (FP; galaxies that are selected to be quiescent, but have specific SFRs above the green-valley threshold in Figure 8) divided by the total number of selected galaxies. Thus, the sample purity is 1−Contamination. We also evaluate the ratio of true-to-false positives (TP/FP) as an additional criterion of efficiency. Note that our definitions of completeness and contamination have different denominators. This is why the contamination rate in Figure 10 is not 50% at $z = 3$ even though the *UVJ* TP/FP ratio is 2.

We see that the $(ugi)_s$ diagram, although comparable in completeness to *UVJ*, has significantly less contamination, hence a much higher TP/FP ratio as a function of redshift. A slightly smaller wavelength baseline in $(u - g)$ and $(g - i)$ means less quiescent galaxies overall are selected in $(ugi)_s$ and *ugi* (hence $(ugi)_s$ is ∼5% less complete) at lower redshifts. At higher redshifts ($z > 2.5$), we start to see the effects of extrapolation and increased contamination from strong [O III] emitters on *UVJ* and *ugi*, problems that the $(ugi)_s$ filters are designed to fix. By $z = 3.5$, the *UVJ* selection has a TP/FP ratio of ∼1, which means that *the contaminants in the UVJ-selected quiescent sample are just as numerous as the true quiescent galaxies*.

SFRs and stellar masses from SED-fitting codes have a persistent 0.5 and 0.2 dex scatter (see Section 2.1.1), respectively. While the flexible SFHs and and self-consistent SED modeling employed in `Prospector-`α and `MAGPHYS` reduce systematics and hence provide an improved ability to mitigate this effect, it is still worth noting. In order to investigate the effect of this offset on our derived completeness and contamination fractions, we repeat our analysis above using SFRs and stellar masses in the 3D-HST catalogs derived using `FAST`, which uses more a simplistic parameterization of the SFH (usually exponential or *delayed exponential* models) and tends to be the traditional choice for estimating stellar population parameters in the literature. Figure 10 (bottom panel) shows the results from these tests. All three methods (*UVJ*, *ugi*, $(ugi)_s$) using `FAST` have lower completeness rates. We attribute this to the adopted SFH, which has been shown to produce highly biased stellar population parameters (e.g., Carnall et al. 2019), favoring young stellar populations, hence higher sSFRs. This particularly impacts red galaxies (which could be either dusty star-forming galaxies or quiescent galaxies) at high-redshift, for which this SFH has been shown to be inadequate (see Section 2.1.2). Nevertheless, the effect appears to be systematic, affecting all color–color methods similarly.

Our results with `FAST` mirror those derived from `Prospector-`α and `MAGPHYS` above: the completeness of quiescent galaxies is similar for all three color–color methods (left column of Figure 10). However, the contamination in the quiescent selection is consistently lower using the $(ugi)_s$ colors at $z > 3$. Finally, the $(ugi)_s$ color selection of quiescent galaxies has the highest TP/FP ratios (right column of Figure 10). This is primarily a result of the lower contamination from the $(ugi)_s$ selection, and for this reason, we see the largest improvement in TP/FP at $z > 3$. This fact will be crucial at these redshifts as contaminants (FP) can otherwise exceed TP, as in *UVJ*.

Our results for the completeness and contamination of *UVJ*-selected quiescent galaxies at $z \leqslant 4$ are broadly consistent with similar results in the literature using photometric data from large area surveys, spectroscopic campaigns, and simulations. Spectroscopic studies at $z < 1$ have shown that *UVJ*-selected quiescent galaxies at various mass cutoffs show ∼10%–65% contamination from galaxies with signs of ongoing star formation (e.g., Tacchella et al. 2022). Using a sample of $\log(M_*/M_\odot) > 10$ galaxies at $1.5 < z < 2.5$ in 3D-HST, Leja et al. (2019b) find that galaxies with the lowest specific SFRs ($\log(\mathrm{sSFR}) < -10.5$) show up to ∼30% contamination. Using CANDELS, Shahidi et al. (2020) find 80% completeness for $\log(M_*/M_\odot) > 10$ galaxies at $2.8 < z < 4$, and 50% completeness at $z = 4$–5.4. Using SHELA (Papovich et al. 2016; Wold et al. 2019), Sherman et al. (2021) find up to 38% contamination from dusty galaxies for $\log(M_*/M_\odot) > 11$

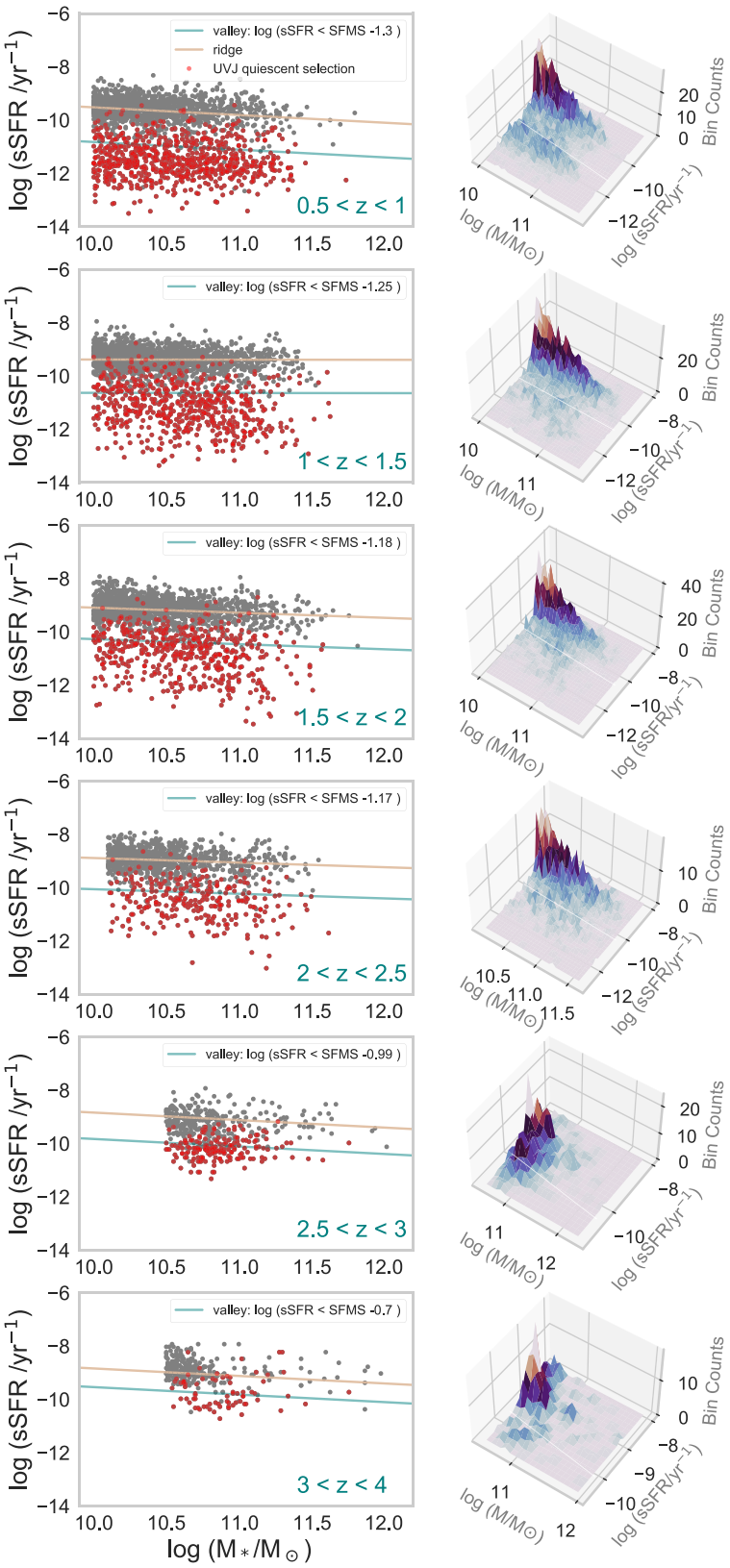

Figure 8. Selection of quiescent galaxies based on specific star formation rate (sSFR). Each row shows the distribution of sSFR as a function of stellar mass in bins of redshift (low-to-high, top-to-bottom). In each row, the left panel shows the selection of quiescent galaxies by identifying the density peak of the star-forming main sequence (SFMS) at each redshift and the green valley between the red and blue sequences, which we define as where the data falls below 10% of the peak. Because our galaxy samples at $z > 2.5$ are small, we use the slope of the SFMS at $2 < z < 2.5$ for the two highest-redshift bins. The mass range at each redshift reflects the 90% stellar mass completeness limit of the 3D-HST ($0.5 < z < 2.5$) and UltraVISTA ($2.5 < z < 4$) surveys. The right panel in each row then shows a 3D projection of the SFMS at each redshift. The white line shows the estimated location of the green valley between the red and blue sequences.

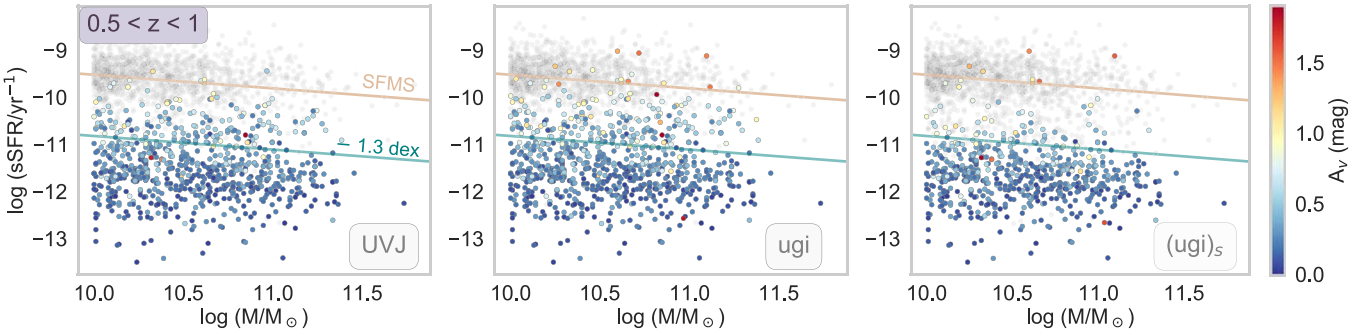

Figure 9. Demographics of quiescent galaxies selected in each method at $0.5 < z < 1$ in 3D-HST. The colored points are the galaxies identified as quiescent in *UVJ*, *ugi*, and $(ugi)_s$. We color-code each sample by dust extinction from `Prospector-`α. Gray points mark galaxies outside of the quiescent region. The *green valley* (teal line) and peak of the star-forming main sequence (brown line) are the same as those from Figure 8 at this redshift. Due to a slightly smaller baseline than *UVJ*, *ugi* and $(ugi)_s$ select a few galaxies with high dust obscuration ($A_V \geqslant 1$), as these tend to lie closer to the diagonal line in these color diagrams than in *UVJ*. The majority of false positives (galaxies above the teal line) have moderate dust extinction values (median $A_V \approx 0.5$) and high specific star formation rates (<-10 yr^{-1}). $(ugi)_s$-selected quiescent samples have less contamination from these dusty galaxies than *UVJ* and *ugi*.

quiescent galaxies at $1.5 < z < 3$. Finally, Díaz-García et al. (2019) find a 20% contamination rate at $z \sim 1$ from the dusty galaxies using data from the ALHAMBRA survey (Moles et al. 2008). Similarly, for the simulations, Lustig et al. (2023) find 67%–75% completeness and 50%–60% contamination for $\log(M_*/M_\odot) > 11$ quiescent galaxies at $z = 2.7$ in Magneticum[18] (Steinborn et al. 2016) and Illustris TNG[19] (e.g., Springel et al. 2018).

Lastly, we would like to caution the reader on the importance of calibrating color-selection methods on the data set that they choose to use for their study. A number of studies, including Kawinwanichakij et al. (2016), have pointed out that there are systematic offsets in the rest-frame colors of galaxies at fixed mass and redshift in different surveys. This means that quiescent selection lines defined on different data sets will yield different numbers of quiescent galaxies, resulting in different completeness and contamination rates. We demonstrate this by applying the Whitaker et al. (2011) and Williams et al. (2009) *UVJ* lines to our data set and reporting their completeness and contamination rates in Figure 10. Although the Whitaker et al. (2011) line appears to be quite similar to ours, the results for the Williams et al. (2009) lines are very different, yielding up to 10% more quiescent galaxies and contaminants. We also determined during some earlier tests that the Muzzin et al. (2013) lines (not shown in Figure 10) yield up to 20% less completeness and 5% less contamination than the other *UVJ* lines applied to our data set. For these reasons, although we provide $(ugi)_s$ lines, we urge the reader to treat them as initial selections and calibrate the color selection lines on their own data set in order for the method to be most accurate.

5.1.2. Results at $z \geqslant 4$: What to Expect with JWST

Using the same methodology and definitions detailed above, we determine the completeness and contamination of the quiescent selections of *UVJ*, *ugi*, and $(ugi)_s$ in simulated JWST data using the JAGUAR catalog (Williams et al. 2018). We do this using a sample of 10,200 galaxies split into two redshift bins: $3 < z < 4$, and $4 < z < 6$. The latter bin is large because there are only a handful of quiescent galaxies in the catalog at these redshifts (TP = 139; Figure 11). For the $z > 4$ bin, we lower the $(U - V)_0$ line by 0.23 mag to include more post-starburst galaxies in the quiescent region, because there is evidence from both photometric and spectroscopic samples at high-z that these galaxies tend to have much lower $U - V$ colors than the quenched population (Marsan et al. 2015; Schreiber et al. 2018; Forrest et al. 2020b; Carnall et al. 2020; Marsan et al. 2022; discussed further in Section 5.3.2). We lowered the horizontal cut by 0.23 mag to match the $U - V$ colors of the young quiescent galaxies in these studies (i.e., $(U - V)_0 \sim 1$). In the same vein, we lower the horizontal lines of the other color-selection methods (*ugi*, $(ugi)_s$) by the same amount.

The completeness, contamination, and TP/FP rates of of the selection methods, *UVJ*, *ugi*, $(ugi)_s$, are shown as a function of redshift from $z = 3.5$, and $z = 6$ in Figure 12. As in Figure 10, although the color-selection methods are comparable in completeness at these redshifts, $(ugi)_s$ has a much lower contamination rate (up to ∼30% less) than *UVJ* and *ugi*, resulting in a higher TP/FP rate ($\gtrsim$2.5). Conversely, *ugi* and *UVJ* have TP/FP rates of $\lesssim$1 by $z = 6$, indicating that the true quiescent galaxies are outnumbered by contaminants, making these methods unfeasible for selecting quiescent galaxies at these redshifts. For this reason, the $(ugi)_s$-selection method provides improved fidelity in color-selected samples of quiescent galaxies at these high redshifts. It is worth noting that these numbers represent the best case scenario, as the number of contaminant dusty star-forming galaxies may be higher in reality, since they tend to be underrepresented in UV-selected samples like JAGUAR (Appendix A).

5.2. Contamination from Extreme-emission-line Galaxies in Quiescent-galaxy Selection

Here, we test the ability of each color-selection method to minimize the number of galaxies with strong emission lines in the quiescent region. Extreme-emission-line galaxies (EELGs) tend to have $EW_0 \sim 100$ Å − 1000 Å in [O II] λλ3726, 3729, Hβ+[O III], and Hα+[N II] although a handful of massive galaxies have been discovered at $z > 7$ with EW(Hβ+[O III]) ≈1000–2000 Å (Smit et al. 2014, 2015; Roberts-Borsani et al. 2016; Castellano et al. 2017). At $z \sim 0.1$, EELGs correspond to rare, starbursting, low-mass galaxies ($\log(M_*/M_\odot) \sim 8$–9) where the mass doubling time can be 100 Myr (e.g., Izotov et al. 2016). These galaxies are 10–100 × more common at $z \gtrsim 1$ (van der Wel et al. 2011; Maseda et al. 2018) than at $z \leqslant 0.5$ and may be the dominant star formation mode at $z = 3$–4 (Kurczynski et al. 2016; Cohn et al. 2018; Tran et al. 2020).

[18] www.magneticum.org
[19] www.tng-project.org

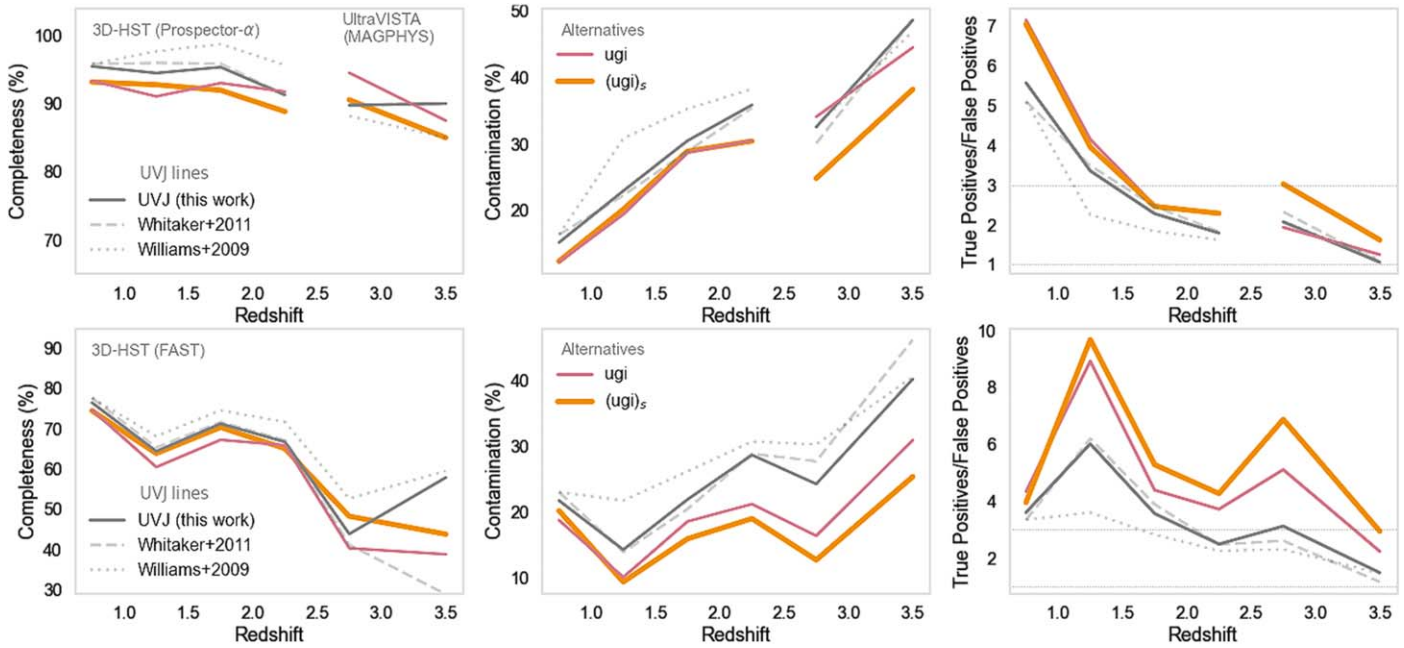

Figure 10. Purity tests of color–color selected quiescent galaxies. The top row shows results using `Prospector-α` fits to the 3D-HST catalogs (Leja et al. 2019c) for galaxies at $z < 2.5$, and the UltraVISTA/`MAGPHYS` catalog (Martis et al. 2019) for galaxies at $z > 2.5$. The bottom row shows results using SFRs and stellar masses from FAST, which is the traditional choice in the literature. In each row, the columns show the completeness (left), contamination (middle), and true-to-false positive ratio (TP/FP) for quiescent galaxies selected by three color–color methods (*UVJ*, *ugi*, and $(ugi)_s$, as labeled). In all cases, we define true quiescent galaxies based on specific SFRs (i.e., by defining the star-forming main sequence in each redshift bin; Section 5). In all cases, we find that the different methods produce similar completeness. However, the contamination of $(ugi)_s$ is up to ∼15% less than that of the other color–color selections. For this reason, the TP/FP ratio is highest for $(ugi)_s$. For example, the TP/FP rate for *UVJ* selection dwindles to ∼1 by $z = 3.5$ (where there is an equal number of false positives for each true positive detected). In contrast, $(ugi)_s$-selected samples have a TP/FP ratio that is nearly a factor of 2 higher.

Galaxies with strong emission lines can mimic the rest-frame *UVJ* colors of galaxies with old stellar populations by boosting their photometry and making them appear redder in $(U - V)_0$ than they actually are (e.g., Labbé et al. 2005). Strong emission lines can be a result of either ongoing star formation or AGN activity, both of which are observed to increase at higher redshifts (e.g., Sobral et al. 2014; D'Eugenio et al. 2020; Marsan et al. 2022). Hβ+[O III] emission with EW ⩽ 200 Å has been shown to boost fluxes in the *K* band[20] by 5%–30% (Schreiber et al. 2018; Forrest et al. 2020a) and in the IRAC bands by up to 65% (Labbé et al. 2013). Based on their central wavelengths and widths, the synthetic u_s and i_s filters require extremely strong lines (rest-frame EW > 800 Å in [O II] and Hα+[N II] respectively) to be contaminated. The synthetic g_s filter, however, has only a 163 Å buffer from the central wavelength of Hβλ4861. This implies that it can be contaminated by galaxies with Hβ+[O III] > 500 Å. While the fraction of star-forming galaxies with Hβ+[O III] EW > 500 Å is low at $z = 1.7$–2.3 (5.4%–8.2%, Boyett et al. 2022), it increases to ∼40% at $z = 5$ (Rasappu et al. 2016 [21]) and could reach ∼50% at $z = 6$, assuming that the rest-frame optical emission evolves as a power law, $(1+z)^P$, and given that fractions at $z \sim 7$ are measured to be ∼65% (Endsley et al. 2021). Consequently, we can expect an increasingly larger number of EELGs to contaminate the quiescent region at higher redshifts by boosting the fluxes in the reddest observed photometric bands (*K*-band − IRAC channel 4).

We quantify this contamination for *UVJ*, *ugi,* and $(ugi)_s$ using mass-complete samples from 3D-HST and JAGUAR at $1.2 < z < 2.3$, and $4 < z < 6$, respectively. The 3D-HST line measurements are from HST/WFC3 G141 grism observations (Momcheva et al. 2016), and those from the simulated JAGUAR catalog are determined using the `BEAGLE` SED fitting code (Williams et al. 2018). In Figure 13, we show the fraction of galaxies in the quiescent region with Hβ+[O III] EWs > 500 Å for all three color-selection methods. For the EW > 500 Å population at both redshift ranges, although the methods have similar fractions of EELGs in their quiescent regions, the $(ugi)_s$ diagram has a smaller number of them (a factor of 1.6 lower). However, for the EW > 300 Å EELG population, the contamination in $(ugi)_s$ is lower by a factor of 3. For comparison, EW > 200 Å contamination fractions at $z > 4$ are as follows: 0.38 (*UVJ*, $N = 92$), 0.22 (*ugi*, $N = 37$), 0.11 ($(ugi)_s$, $N = 14$). Photometric redshift uncertainties could also be a factor (as an erroneous redshift could shift an emission line into the rest-frame band, although this effect will be lessened for galaxies with stronger emission lines as these tend to have lower-redshift uncertainties; see Momcheva et al. 2016). Nevertheless, in Appendix B, we show that photometric redshift errors of $\sigma_z/(1+z) < 9.1\%$ correspond to fewer than 16% of sources having their rest-frame colors impacted by emission lines (and most modern surveys have better photometric redshift accuracy than this). Therefore we do not expect this to significantly impact the rest-frame colors. Our results are consistent with spectroscopic surveys, which report a contamination rate of 21%–30% from EW(Hβ+[O III]) > 100 Å galaxies in *UVJ*-selected quiescent samples at $z = 3$–4, with at least a third of those having $f_{[O\ iii]}/f_{H\beta} > 6$ (Schreiber et al. 2018; Forrest et al. 2020a), indicative of AGN activity, particularly at high mass (e.g., Belli et al. 2017; Strom et al. 2017; Reddy et al. 2018). In Appendix C, we show that $(ugi)_s$ screens all of the star-forming contaminants in *UVJ* and *ugi* at $3 < z < 4$.

[20] Originally shown by Shapley et al. (2005).
[21] Converted from EW(Hα) by Boyett et al. (2022).

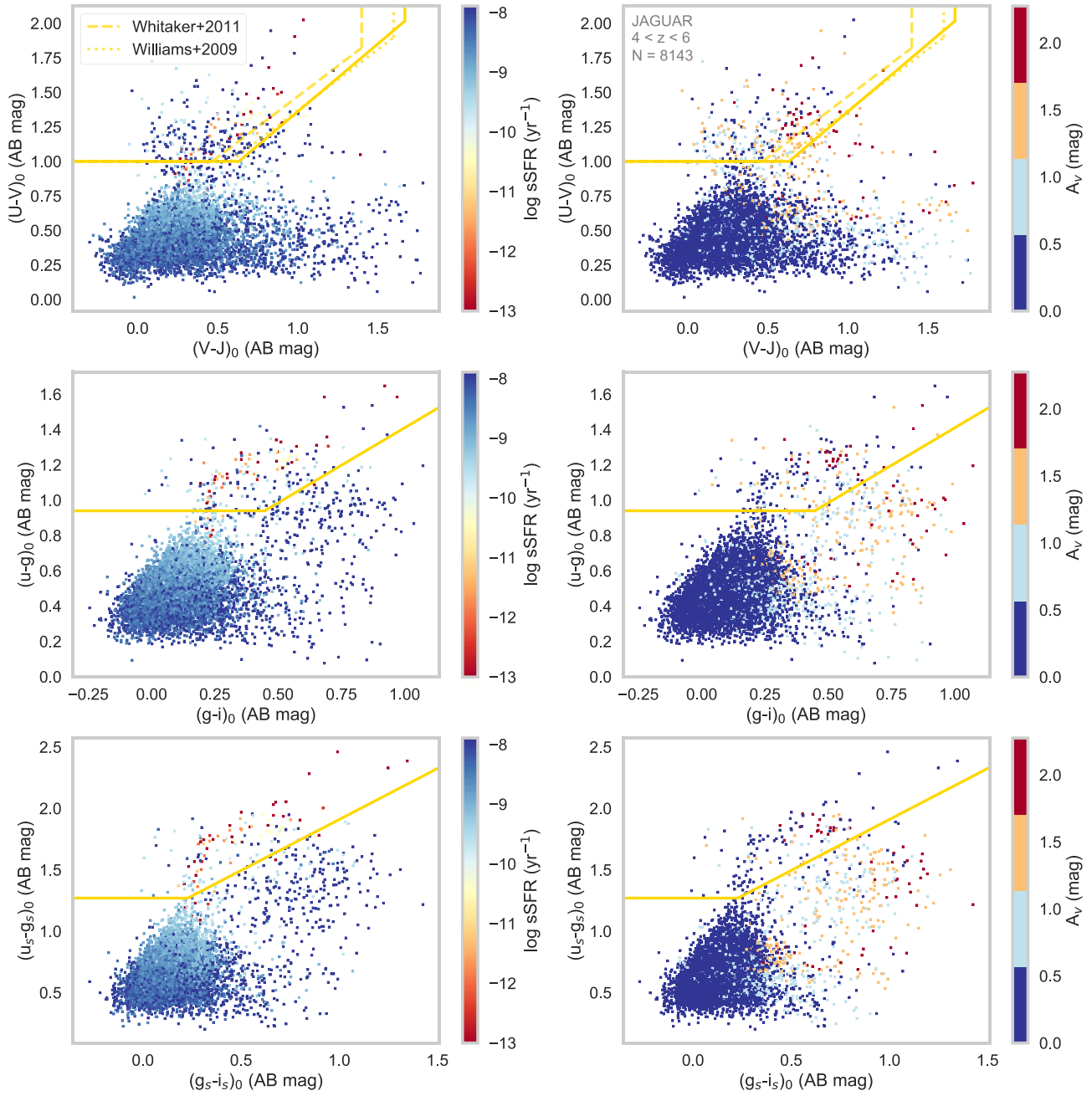

Figure 11. Color-color diagrams for simulated data with added noise at $4 < z < 6$. Each row shows color–color diagrams for galaxies with $\log(M_*/M_\odot) \geqslant 8.9$ in the JAGUAR catalog, color-coded by specific star formation rate (left panel in each row), and dust extinction (right panel in each row). The top row shows the *UVJ* colors. The middle row shows the *ugi* colors. The bottom row shows the $(ugi)_s$ colors. In each case, the rest-frame colors were derived using HST, JWST/NIRCam, and *Spitzer*/IRAC photometry from 0.4 to 5 μm. The $(U-V)_0$, $(u-g)_0$, and $(u_s-g_s)_0$ horizontal lines were each lowered by 0.23 mag to accommodate the increasingly younger population of quiescent galaxies at these redshifts, although we maintained the slopes and zero-points from Figure 3.

5.3. Implications for Quiescent-galaxy Selection at z > 4: Current and Future

5.3.1. The Beginning of the End

We are approaching the end of the era of discovery of quiescent galaxies. We have spent the past two decades attempting to obtain a complete census of different populations of galaxies as a function of redshift, and color-selection methods have played a pivotal role in this (e.g., Daddi et al. 2004; Quadri et al. 2007; Kriek et al. 2009; Guo et al. 2013; Nayyeri et al. 2014). Color-selection methods are useful because they can quickly isolate different galaxy populations in large data sets over a range of redshifts using only 3 bands. Although star-forming galaxies may well exist out to $z \sim 13$ (Harikane et al. 2022), we may be reaching the era where there are no more quiescent galaxies to be selected ($z \sim 6$). We have spectroscopically confirmed quiescent galaxies out to $z \sim 4$ (Cimatti et al. 2004; McCarthy et al. 2004; Marsan et al. 2015; Glazebrook et al. 2017; Tanaka et al. 2019; Forrest et al. 2020b; Saracco et al. 2020; Valentino et al. 2020), and we have a handful of photometrically selected candidates at $z = 5 - 6$ (e.g., Mawatari et al. 2016; Merlin et al. 2019; Marsan et al. 2021)

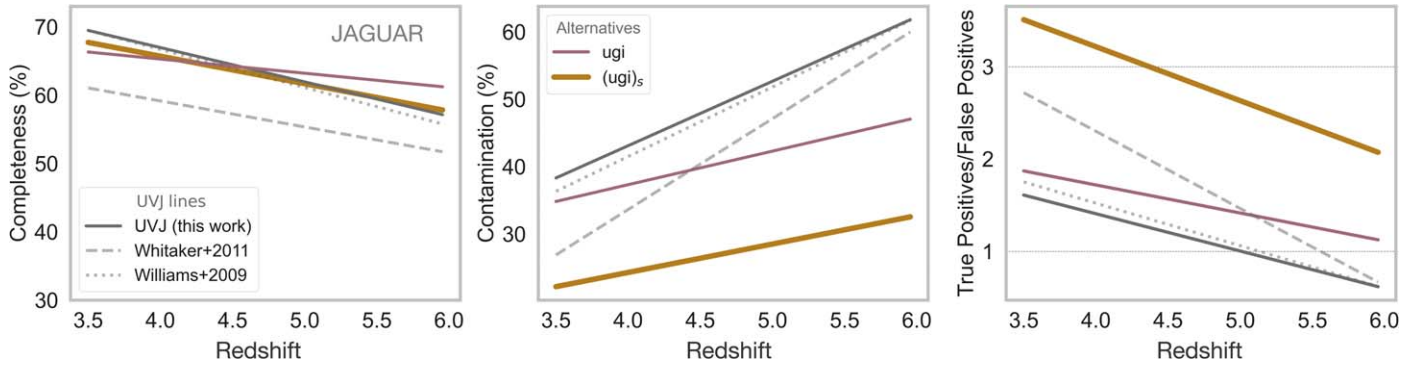

Figure 12. Sample selection efficiency of *UVJ*, *ugi*, and $(ugi)_s$ at $3 < z < 6$. We show the completeness and contamination of the quiescent selections of *UVJ*, *ugi*, and $(ugi)_s$ using specific star formation rates from the JAGUAR catalog, which were generated using BEAGLE. As in Figure 10, although the color-selection methods are comparable in completeness at these redshifts, $(ugi)_s$ has a much lower contamination rate (up to ∼30% less) than those of *UVJ* and *ugi*, resulting in a higher true-to-false positive rate at $z = 6$ ($\geqslant$2.3). Conversely *ugi* and *UVJ* have true-to-false positive rates of $\lesssim$1 by $z = 6$, indicating that the true quiescent galaxies are outnumbered by contaminants, making these methods unfeasible for selecting quiescent galaxies at these redshifts.

with searches underway using ground-based surveys that leverage the detection capabilities of medium-band filters (Esdaile et al. 2021). However, given that passive fractions are <10% at $z > 4$ (e.g., Santini et al. 2021), by $z \sim 6$, we will be witnessing the emergence of the first quiescent galaxies. These quiescent galaxies will be some of the first to have started forming stars and quench and will be important for answering questions about structure formation in the early universe and settling debates about quenching mechanisms (see Nanayakkara et al. 2022 for a review). With this in mind, it is ever so important that we select pure and complete samples of quiescent galaxies for spectroscopic follow-up so that we do not miss any of this interesting population.

In this paper, we have presented three synthetic filters: u_s g_s, and i_s, which accomplish this goal most efficiently, using data from our largest and deepest ground-based photometric surveys and simulated JWST data. We consider one of our intended goals in designing our filter set, achieving increased sensitivity to the Balmer/4000 Å break. In Figure 14, we show the distribution of the vertical colors of galaxies in the quiescent regions of *UVJ*, *ugi* and $(ugi)_s$ at $1.2 < z < 2.3$, and $4 < z < 6$. The strength of the Balmer break is predicted to be lower at fixed sSFR for galaxies at $z = 2$–10 than for their lower-redshift counterparts (Shen et al. 2020). If so, we expect the vertical colors in the high-z bin to be bluer than those in the low-z bin and that the most efficient color-selection method would have redder vertical colors overall, signaling that the Balmer/4000 Å break produces a stronger color signature in that color space. This is precisely what we see in Figure 14, with median values of $(u_s - g_s)_0 = 1.73$, $(U - V)_0 = 1.19$, and $(u - g)_0 = 1.13$ at $z > 4$. A wider range in $(u_s - g_s)_0$ ($\sigma_{\rm NMAD} = 0.19$) over $(U - V)_0$ (0.15) and $(u - g)_0$ (0.13) at those redshifts may also indicate that $(ugi)_s$ is better at capturing the diversity of quiescent SEDs at higher redshift than *UVJ* and *ugi*. Indeed, galaxies enter the quiescent region at younger ages in $(ugi)_s$ than those in *UVJ* and *ugi* (∼250 and 150 Myr younger, respectively in Figure 15), which allows $(ugi)_s$ to select young post-starbursts typically missed in *UVJ* selection (Figures 16 and 17). This property will be extremely useful for studying the age gradients of the first quiescent galaxies (e.g., Whitaker et al. 2013).

This is particularly important because, so far, most of the quiescent galaxies that have been confirmed spectroscopically at $z > 3$ are young, recently quenched galaxies, with a few exceptions (e.g., Galaxy D in Kalita et al. 2021). Older quiescent galaxies are predicted to be 1–2 mag fainter in the *K* band than their post-starburst counterparts at the same redshift, with stronger Balmer/4000 Å breaks and weaker absorption lines due to their evolved stellar populations (Forrest et al. 2020b). This suggests that their absence from current surveys is simply a selection effect; therefore this population should be revealed with deep ongoing NIR surveys, e.g., FENIKS (Esdaile et al. 2021) and the upcoming JWST ERS, GTO, and GO programs, which will enable us to detect some of the faintest galaxies in the distant universe.

5.3.2. Possible Limitations of the $(ugi)_s$ Diagram

Next, we consider an apparent limitation of $(ugi)_s$, and color–color selection methods in general at high-z. If indeed $(ugi)_s$ is more efficient at selecting high-z quiescent galaxies, why then is it $\lesssim$70% complete at $z > 4$ (Figure 12)? First, the simplest explanation is that they were scattered out of the quiescent region due to the addition of noise, because that would preferentially affect faint and low-mass galaxies. In fact, the completeness of quiescent galaxies is reduced by ∼20% for all three methods after we add noise (Appendix A).

A second possibility is that we are missing some quiescent galaxies because our adopted slope for the $(ugi)_s$ diagonal line excludes them. For the sake of consistency, we assumed that the slope of the diagonal line remains constant as a function of redshift, similar to what others have done (Williams et al. 2009; Whitaker et al. 2011; Muzzin et al. 2013). Like those studies, we lowered the horizontal cut to account for the evolution in color due to quiescent galaxies having increasingly younger ages at higher redshifts (see discussion in paragraph below). However, it is not entirely clear if the slope needs to evolve as well, particularly at $z > 3$. This can be resolved with larger unbiased samples of quiescent galaxies with high signal-to-noise photometry.

A third possibility is that lowering the horizontal lines of each color diagram by 0.23 mag is not enough to capture all the post-starbursts in the sample. This would be the case for dust-free star-forming galaxies that quenched abruptly (<175 Myr) prior to observation, as they can have $(U - V)_0$ colors as low as 0.5 mag (Merlin et al. 2018), which suggests that genuinely quiescent galaxies can be found outside of the fiducial *UVJ* boundaries, and by extension, the $(ugi)_s$ boundaries as well. For example, the 320 Myr old post-starburst galaxy in Forrest et al. (2020a) is missed in both *UVJ* and $(ugi)_s$ (Figures 19 and 20).

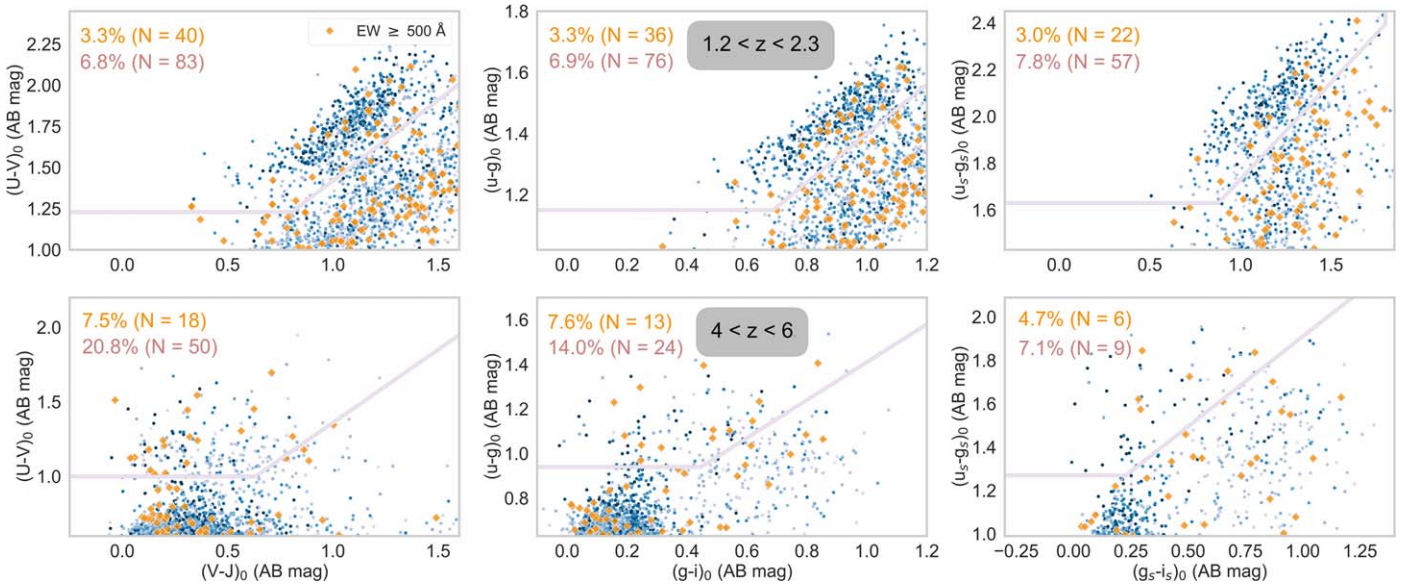

Figure 13. Fraction of extreme-emission-line galaxies in *UVJ*, *ugi*, and $(ugi)_s$ using mass-complete samples from 3D-HST and JAGUAR at $1.2 < z < 2.3$ (top), and $4 < z < 6$ (bottom), respectively. For each redshift bin, each color diagram shares the same line parameters as Figure 11. As in Figure 11, the ordinate limits and horizontal color lines shown are different for each diagram in order to capture the evolution of galaxies in color space as a function of redshift. The fractions and numbers of rest-frame EW > 500 Å galaxies selected as quiescent in each color diagram are shown in orange. For the EW > 500 Å population in both redshift bins, although the methods have similar fractions of EELGs in their quiescent regions, the $(ugi)_s$ diagram has a smaller number of them (a factor of 1.6 lower). We also show the numbers and fractions of EW > 300 Å in brown (not plotted) for comparison. For the EW > 300 Å EELG population, the contamination in $(ugi)_s$ is lower by a factor of 3.

Metal-poor galaxies ($Z = 0.02\,Z_{\odot}$), which take ~3 Gyr to become *UVJ*-quiescent, also meet this fate, as the time needed to enter the quiescent region exceeds the age of the universe at that redshift (Tacchella et al. 2018). Post-starburst galaxies are predicted to comprise an increasingly larger fraction of the quiescent population at $z > 3$ because the galaxies will have less time to evolve passively after quenching. One possible solution is to use a slightly redder u_s filter ($\lambda_c = 3200$ Å, as opposed to 2900 Å) at $z > 4$. This would produce a stronger $(u_s - g_s)_0$ color signature for the entire quiescent population, potentially moving more post-starbursts into the quiescent region. This, however, may be at the risk of increasing the contamination from dusty star-forming galaxies, as this modification would reduce the wavelength baseline needed to accurately measure the dust reddening in the NIR. Others have resolved this by eliminating the horizontal $(U - V)$ cut altogether and instead extending the diagonal line to bluer colors (e.g., Forrest et al. 2020a; Marsan et al. 2022). While this would increase the number of post-starbursts in the quiescent region, it would also, unfortunately, increase the number of nondusty star-forming contaminants. It is also important to note that the way the slope of the diagonal line is determined becomes even more critical in this case (see our cautionary note in Section 5.1.1).

The fourth and final possible reason for <70% completeness at $z > 4$ is that we may be missing old galaxies that are significantly obscured by dust ($E(B\text{-}V) \gtrsim 0.4$, i.e., $A_V \gtrsim 1$), causing them to fail the $V - J$ (hence the $(g_s - i_s)_0$) cut (Merlin et al. 2018). Although the local ($z \sim 0$) massive, quiescent galaxies have little-to-no dust (Smith et al. 2012), recent observations have shown that their quiescent counterparts at higher redshifts ($z \gtrsim 1.5$) could be dusty, with up to 12% showing MIPS and Herschel detections at $z = 3$–4 (Martis et al. 2019). This estimate does not take into consideration gas depletion timescales, which are reported to be quite short (100–600 Myr) for quiescent galaxies at $z \sim 1.5$–3 (Whitaker et al. 2021a; Caliendo et al. 2021; Williams et al. 2021). It may still be possible to catch a quiescent galaxy in its dusty phase if the quenching timescale is longer than the gas depletion timescale. A few galaxies with some measure of dust obscuration (verified via Atacama Large Millimeter/submillimeter Array detections) have been reported in the literature (Schreiber et al. 2018; Whitaker et al. 2021b) and found in simulations (Akins et al. 2022). While it is possible that these galaxies may indeed represent an evolutionary phase for quiescent galaxies, it is equally likely that they are dusty star-forming galaxies masquerading as quiescent galaxies due to their low sSFRs (heavily dependent on the choice of SFH, e.g., Marchesini et al. 2010).

We can resolve this through targeted spectroscopic campaigns searching for the presence (or lack) of absorption features, which would unambiguously confirm their quiescent nature. Additionally, flexible SFHs and self-consistent SED modeling are recommended because they have been shown to better approximate stellar masses as they account for emission from old stars (Leja et al. 2019c; Martis et al. 2019), thereby resulting in more accurate sSFRs for dusty star-forming galaxies and lower dust masses for quiescent galaxies (Whitaker et al. 2021b). In summary, if this population of high-z dusty quiescent galaxies is real, removing the vertical $(g_s\text{-}i_s)$ color cut (e.g., Martis et al. 2019; Marsan et al. 2022) would increase completeness, but would also increase contamination from dusty star-forming galaxies.

It is also important to note that completeness rates are subject to how quiescence is defined (i.e., the estimated location of the SFMS and green valley; see Section 5.1 for a thorough discussion). We find that *none* of the low sSFR galaxies (sSFR < SFMS −0.7) at $3 < z < 4$ that were missed in $(ugi)_s$ are truly quiescent (Figures 19 and 20). This means that we have underestimated our completeness rates at $3 < z < 4$ and may be >70% complete at $z > 4$. One possible solution to this is to consider the $M_* - SFR$ uncertainties for each galaxy when

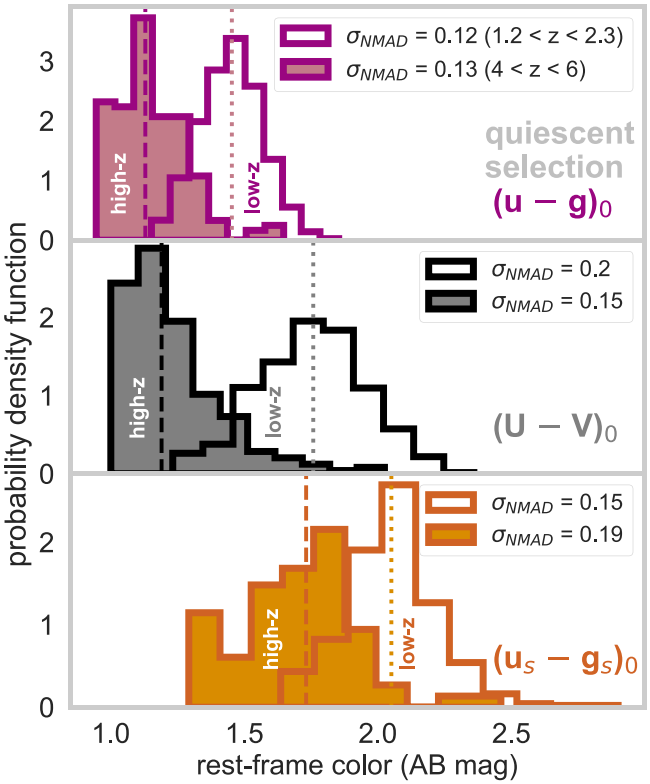

Figure 14. Vertical color of the red sequence in each color-selection method at low and high redshift ($1.2 < z < 2.3$, and $4 < z < 6$) for *ugi* (top), *UVJ* (middle), and $(ugi)_s$ (bottom). The associated median and normalized median absolute deviation for each distribution are also shown. Galaxies at $z < 2.3$ (low-z) tend to exhibit redder colors than those at $z > 4$ (high-z) because the strength of the Balmer/4000 Å break decreases as a function of redshift. The $(u_s - g_s)_0$ color, however, is reddest in both bins, with a median of 1.73 mag (2.05) at $z > 4$ ($z < 2.3$), compared with 1.19 mag (1.76) in $(U - V)_0$ and 1.13 (1.45) mag in $(u - g)_0$. $(ugi)_s$ also has a larger spread in colors. Both of these indicate that $(ugi)_s$ is better at isolating quiescent galaxies and capturing the diversity of quiescent SEDs in the high-z universe.

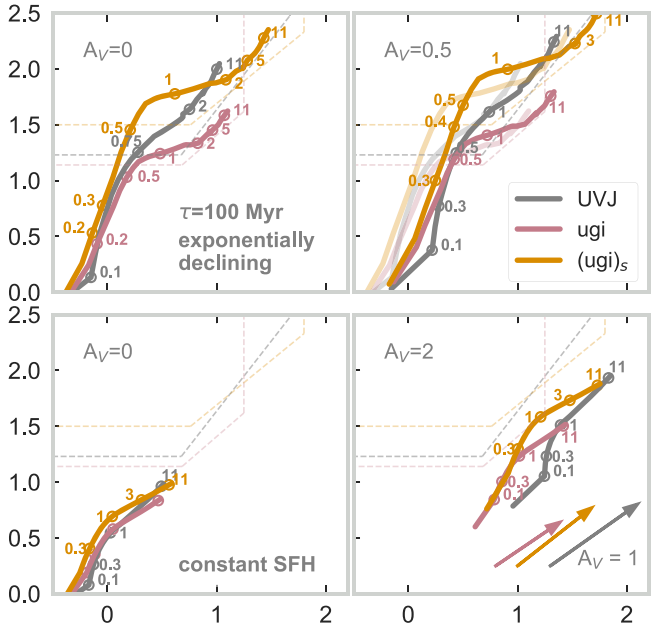

Figure 15. Superimposed color evolution tracks from Figure 2 for *UVJ*, *ugi*, and $(ugi)_s$. Top: tracks for an exponentially declining SFH with e-folding time $\tau = 100\ Myr$ with no dust (left), and $A_V = 0.5$ (right). We also show the dust-free tracks in this panel for reference. Bottom: constant SFH with no dust (left), and $A_V = 2$ (right). All tracks assume a Calzetti et al. (2000) dust extinction curve. Top left: the $\tau = 100\ Myr$ stellar population track evolves into the quiescent region at younger ages in $(ugi)_s$ than those in *UVJ* and *ugi* (~250 and 150 Myr younger, respectively). Top right: moderate dust extinction causes the color tracks to enter the quiescent region at younger ages in all three methods. While this would cause star-forming galaxies to enter the quiescent sample, $(ugi)_s$ is better at reducing contamination from galaxies with strong emission lines. This is likely why it selects fewer moderately dusty galaxies (see Figure 9).

estimating the star-forming density peak (e.g., Leja et al. 2022). This is particularly important for the high-mass end, where (1) a large fraction of galaxies have relatively low SFRs (hence higher SFR uncertainties) and (2) there are few galaxies in total (so the the uncertainties become even more important). Another solution is to consider using a double power-law fit to the SFMS, which allows more flexibility at high masses.

To conclude, we consider the utility and accuracy of color-selection methods compared to others in the literature. Are there better ones out there? The short answer is yes. The longer answer is no. Other methods such as template fitting (e.g., Shahidi et al. 2020) and unsupervised machine-learning algorithms, e.g., t-distributed stochastic neighbor embedding (t-SNE, Steinhardt et al. 2020), are able to use a larger portion of the SED information to classify galaxies, as opposed to only a select few bands. They have been shown to achieve this task quite well, boasting ~80% completeness and <30% contamination at $z < 2$. One major drawback of these methods is that they are computationally intensive and relatively complex (particularly those that employ nonparametric flexible models, e.g., Leja et al. 2019a). Color selection, on the other hand, is convenient and accessible, especially as many catalogs now come with precomputed rest-frame colors.

Additionally, their performance hinges upon the availability of several photometric points, which is a luxury that many surveys with the next generation of telescopes (e.g., Euclid, the Vera Rubin Observatory, and the Nancy Grace Roman Space Telescope) will not have. This will also be the case for JWST observations in new fields, as these will have no existing ancillary data from other catalogs. Lastly, these alternative methods are model-dependent. SED-fitting depends on using galaxy templates that capture the variety of galaxies in the universe, and machine-learning methods must be trained on large, representative samples of galaxies. Both of these are typically available at lower redshifts ($z < 3$), and for several reasons (outlined above), we cannot assume that the quiescent galaxies at low-z resemble those at high-z enough for these methods to be effective. When rest-frame colors are derived either directly from the observed photometry or using empirically derived templates, as we have done in this paper (Sections 2 and 4), they are not subject to the underlying assumptions and biases associated with these model-dependent methods, hence are more representative of reality. We argue that this will remain important through the JWST era.

Going forward, progress in the study of galaxies over cosmic time will likely continue to rely heavily on color selection techniques, both to distinguish between different galaxy populations and to identify targets for spectroscopy. Over the next few months, JWST will provide a rapid and extremely efficient spectroscopic test[22] of quiescence and hence of the $(ugi)_s$ color-selection method. In the meantime, the next step is

[22] The cost of confirming quiescence at $z > 3$ comes out to ~$250 per object, assuming 15 hr of integration with Keck/MOSFIRE. With JWST/NIRSPEC, this will be reduced to ~1 hr and ~$10 per object (assuming a 5 yr mission).

to standardize these independent observational results and bring them to a common scale by using a single color–color selection method over a range of redshifts, and we have demonstrated that the $(ugi)_s$ diagram can do that efficiently. In a follow-up paper, we will explore the distribution of galaxy properties at a range of redshifts in color–color space, comparing the global properties of star-forming and quiescent galaxies (e.g., stellar mass, SFR, number density, IR luminosity, stellar age, and morphology) of $(ugi)_s$ as has been done for *UVJ* (e.g., Williams et al. 2010; Patel et al. 2012; Price et al. 2014; Spitler et al. 2014; Straatman et al. 2014; Leja et al. 2015; Forrest et al. 2016; Martis et al. 2016; Fang et al. 2018; Belli et al. 2019).

This work benefited from the generous support of the George P. and Cynthia Woods Mitchell Institute for Fundamental Physics and Astronomy at Texas A&M University. This material is based upon work supported by the National Science Foundation under grants AST-2009632 and AST-2009442. C.M.S.S. acknowledges support from Research Foundation - Flanders through Fellowship 12ZC120N.

Based on observations taken by the 3D-HST Treasury Program (HST-GO-12177 and HST-GO-12328) with the NASA/ESA Hubble Space Telescope, which is operated by the Association of Universities for Research in Astronomy, Inc., under NASA contract NAS5-26555 and data products from observations made with ESO Telescopes at the La Silla Paranal Observatory under ESO program ID 179.A-2005 and on data products produced by TERAPIX and the Cambridge Astronomy Survey Unit on behalf of the UltraVISTA consortium. This research made extensive use of NASA's Astrophysics Data System for bibliographic information.

J.A.D. would like to thank Gabe Brammer for help with troubleshooting and running his SED-fitting code `eazy-py`, Justin Spilker and Rob Kennicutt for insightful discussions, and Taylor Hutchison and Jonathan Cohn for their help and support throughout the preparation of this manuscript. We are grateful to the anonymous referee whose feedback resulted in extremely valuable additions to the paper.

Data Availability: The synthetic $(ugi)_s$ filters are available on Github.[23] Other data products can be provided upon request to the corresponding author.

Software: `Astropy` (Astropy Collaboration et al. 2018), `eazy-py` (Brammer 2021), `Jupyter` (Kluyver et al. 2016), `matplotlib` (Hunter 2007), `numpy` (Harris et al. 2020), `pandas` (The Pandas Development Team 2020), `seaborn` (Waskom 2021), `scipy` (Virtanen et al. 2020), `statsmodels` (Seabold & Perktold 2010).

Appendix A
Estimating Noise and Creating a Sample of Dusty Star-forming Galaxies in JAGUAR

Williams et al. (2018) generated number counts of star-forming galaxies at $z > 4$ in JAGUAR using UV luminosity functions, rather than stellar mass functions (Section 2.2). Dusty star-forming galaxies, however, tend to be under-represented in UV-selected samples. Observations suggest that they comprise ∼50%–60% of the $\log_{10}\ (M_*/M_\odot) > 10.5$ population at $z = 2$–3 (Martis et al. 2016), and ∼40%–50% at $z = 3$–4 (Spitler et al. 2014; Martis et al. 2019). JAGUAR features ∼20% at these redshifts, a factor of at least 2 lower than what we expect from observations. This becomes problematic for evaluating completeness and contamination fractions of color-selected quiescent samples, as dusty star-forming galaxies are their primary contaminants.

To resolve this, we artificially introduce more dusty star-forming galaxies into the JAGUAR catalogs by doing the following. For a subsample of galaxies with $A_V \geqslant 1$ and $\log(\mathrm{sSFR/yr}) \geqslant -9.5$, we determined the UV extinction at 1500 Å as a function of stellar mass using the following relation from Pannella et al. (2009) for $\log(M_*/\mathrm{M}_\odot) \geqslant 10.1$ star-forming galaxies at $z \approx 2$, assuming that it does not evolve from $z = 2$–6.

$$A_{1500} = 4.07 \times \log(\mathrm{M}_*) - 39.32. \tag{A1}$$

For the low-mass ($\log(M_*/\mathrm{M}_\odot) \leqslant 10.1$), we assume $\mathrm{A}_{1500} = 1$ mag (Salim et al. 2005). We applied 1 mag of scatter to A_{1500}, using a lognormal distribution to prevent the perturbed extinction values from going negative. Using the UV extinction, we estimated the color excess for each galaxy using the reddening curve from Calzetti et al. (2000):

$$E(B-V) = \frac{A_{1500}}{k(1500)}. \tag{A2}$$

The extinction as a function of wavelength, $\mathrm{A}(\lambda)$, can then be obtained from the color excess, and the reddened flux in each bandpass is:

$$f_{\nu,\mathrm{reddened}} = 10^{\frac{2.5\log(\mathrm{f}_\nu)+\mathrm{A}(\lambda)}{2.5}}. \tag{A3}$$

We add uncertainties to the HST and JWST photometry using publicly available code made for the JAGUAR catalogs (Hainline et al. 2020). For a user-specified survey depth, the code estimates noise directly from the photometry by determining the total flux in the smallest fixed aperture between $r = 0\farcs16$ and $r = 0\farcs64$ that matches the galaxy's half-light radius, estimated using the Sérsic index of the galaxy. The uncertainty on the flux in each band is then given as the Poisson noise and the instrument read noise summed in quadrature. We determine the final noise estimate per band (for each galaxy) as a random draw from a Gaussian with a width set to the uncertainty on the flux. We show the *UVJ*, *ugi*, and $(ugi)_s$ diagrams for $\log(M_*/M_\odot) \geqslant 8.9$ galaxies at $4 < z < 6$ using the perturbed data in Figure 11. The mass cutoff is based on the expected mass completeness limit at $z = 6$ for the Cosmic Evolution Early Release Science (CEERS; P.I.: S. L. Finkelstein) survey (Kauffmann et al. 2020).

The addition of noise preferentially affects low-mass ($\log(M_*/M_\odot) < 10$) and faint galaxies, causing them to scatter in and out of the quiescent region. The completeness of the perturbed sample is lower by ∼10% from the original at $z = 3$–4, and ∼20% at $z = 4$–6. The contamination rates after the addition of noise are similar to that of the unperturbed sample.

Appendix B
Effect of Photometric Redshift Uncertainty on Contamination from Strong Emission Lines

In Section 5.2 and Figure 13, we presented an estimate of the fraction of EELG contaminants in the quiescent selection of each color selection using a sample of galaxies at low-z ($1.2 < z < 2.3$) and high-z ($4 < z < 6$). We demonstrated that

[23] https://github.com/jacqdanso/synthetic-ugi-filters

Table 2
Photometric Redshift Uncertainties Required for the Strongest Emission Lines to Contaminate the Synthetic Filters

Synthetic Filter	Filter Edge (Å)	Emission Line	Rest Wavelength[a] (Å)	Buffer[b] (Å)	σ_z[c]	Δz (at $z = 3$)
u_s	3100 (R)	[O II]	3729.875	627	0.249	−0.996
g_s	4300 (L)	[O II]	3729.875	573	0.228	0.912
g_s	4700 (R)	Hβ	4862.68	163	0.048	−0.192
g_s	4700 (R)	[O III]	4960.295, 5008.24	307	0.091	−0.364
i_s	7000 (L)	Hβ+[O III]	4862.68, 4960.295, 5008.24	2993[d]	0.885	3.54
i_s	7000 (L)	Hα+[N II]	6564.61, 6585.27	452	0.102	0.408
i_s	8000 (R)	Si III	9068.6, 9530.6	1069	0.174	−0.698

Notes.
[a] Vacuum rest-frame wavelengths obtained from Momcheva et al. (2016) and the SDSS database (http://classic.sdss.org/dr6/algorithms/linestable.html).
[b] Wavelength separation between the central wavelength of the line and filter edge, used to determine $\lambda_{\rm new}$ in Equation (B3).
[c] Photometric redshift scatter, given by Equation (B3).
[d] Conservative estimate using Hβλ4863.

their fractions in the $(ugi)_s$-selected quiescent samples are lower by a factor of 1.6–3.5 than that of *UVJ* at these redshifts, where the fraction of star-forming galaxies with rest-frame EW > 500 Å is expected to be ≃10%–50% (Boyett et al. 2022). Underlying these estimates, however, is the assumption that we have precise and accurate photometric redshifts. For the 3D-HST sample, the maximum photo-z scatter (based on spectroscopic redshifts up to z ∼ 6) is 2.6% (Skelton et al. 2014), and that for JAGUAR is effectively 0%, since it is simulated data. In reality, redshift uncertainties for ground- and space-based photometric surveys may be higher.

In this section, we consider the effect of photometric redshift uncertainty. We do this by estimating the photometric redshift uncertainty required for the strongest emission lines to shift into the synthetic filters (that is, we translate the wavelength shift required for a given emission line to contaminate a specified synthetic filter into a 1σ uncertainty on the redshift). Photometric redshift scatter is typically reported as the normalized median absolute deviation:

$$\sigma_{\rm NMAD} = 1.48 \times median\left(\frac{\Delta z}{1 + z_{\rm true}}\right) \quad \text{(B1)}$$

where $z_{\rm true}$ is often determined using spectroscopy. Given an emission line that has shifted into a photometric bandpass

$$\lambda_{\rm new} = \lambda_{\rm orig}(1 + z + \Delta z); \quad \text{(B2)}$$

the photometric redshift scatter required for the line to contaminate a given filter is

$$\sigma_z = 1.48 \times \left(\frac{\lambda_{\rm new} - 1}{\lambda_{\rm orig}(1 + z)}\right). \quad \text{(B3)}$$

We report our results for the four strongest emission lines in Table 2. For blended lines and doublets, we make conservative estimates by using the central wavelength of the emission line closest to the synthetic filter in question. Based on our calculations, the filter most likely to get contaminated is g_s with Hβ+[O III]. Due to the proximity of these emission lines to the filter, small photo-z uncertainties (≃5%–9%) can cause the lines to scatter into the g_s filter and artificially boost the $(u_s - g_s)_0$ color. Is this enough to warrant concern? Medium-band photometric surveys such as ZFOURGE (Straatman et al. 2016) and NMBS (Whitaker et al. 2011) boast 1%–2% photo-z uncertainties due to finer sampling of the SED. Deep NIR surveys such as UltraVISTA (Muzzin et al. 2013) that include medium-band photometry from the aforementioned also report similar uncertainties up to $z \sim 2$. Typical photo-z uncertainties are on the order of 5% (e.g., COSMOS2020; Weaver et al. 2022). Similarly, photo-z uncertainties of 5%–8% are expected for the faintest objects ($m_{F200W} > 24$ AB) in upcoming photometric surveys with JWST such as CEERS (Kauffmann et al. 2020). Since these estimates are well within our redshift uncertainty tolerance for the g_s filter, the contamination from galaxies with strong emission lines will likely be small compared to *UVJ*, as we have demonstrated in Section 5.2.

A reasonable critique of this conclusion is that photo-z uncertainties from ground-based surveys are underestimated, as they are usually evaluated using galaxies with spectroscopic redshifts. These are typically highly biased samples, comprising only ∼1% of the catalog and tend to be 2–5 mag brighter than the rest of the sample. Our counter is that, for precisely this reason, EELGs will have some of the most precise redshifts in the sample, as they tend to be bright, and the presence of emission lines makes it easier to obtain spectroscopic redshifts for them. Additionally, many SED fitting codes (including `eazy-py`) now include EELG templates in order to account for the effects of emission lines on the observed photometry (see Section 2.3). One way to test the accuracy of the photometric redshift uncertainties from our sample in 3D-HST is to look at the predicted change in magnitude caused by a contaminating emission line. Because g_s is much narrower than V ($\Delta\lambda = 400$ Å versus 991 Å), a stronger magnitude change is introduced in g_s than in V when contaminated by an emission line (Equation (1)). This means that if the photo-z uncertainty exceeds our estimated threshold, there should be more galaxies with moderate Hβ+[O III] line strengths (EW > 200 Å) in the $(ugi)_s$ quiescent region than that for *UVJ*, since they will produce a strong magnitude change of (1.93 mag) in the former and a relatively weaker one in the latter (0.64 mag). What we see is the opposite, with the number of EW > 200 Å galaxies in $(ugi)_s$ being a factor of ≃1.4 less than that in *UVJ* (92 as opposed to 130). This suggests that the photometric redshift estimates in 3D-HST have an uncertainty of <5% and lends credibility to using spectroscopic redshifts for estimating photometric redshift uncertainties.

Appendix C
Demographics of Quiescent Selections and Contaminants of Each Method

Here, we sketch out the types of galaxies that are missing in $(ugi)_s$ selection and those that erroneously enter the sample. In particular, we answer the following questions: What galaxies are we missing, and why? How are they biased relative to those selected? What are the FP, and why are we selecting them? To do this, we looked at galaxies at $3 < z < 4$ in UltraVISTA, as the effects of extrapolation (Section 4), and the contamination from galaxies with strong emission lines (Section 5.2) start to become more important at those redshifts. We show the SEDs and stellar population parameters of these galaxies, derived by fitting their UV–far-IR photometry with MAGPHYS (Section 2.1.2).

Our main conclusions are summarized as follows:

1. $(ugi)_s$ selection captures recently quenched galaxies at younger ages than those of *UVJ* and *ugi*. This is evident from the color evolution tracks in Figures 2 and 15, with the $\tau = 100\,Myr$ line, also referred to as the "fast-quenching" track (e.g., Belli et al. 2019), entering the $(ugi)_s$ quiescent region ∼250 and 150 Myr earlier than those in *UVJ* and *ugi*, respectively. In Figure 16, we show that the galaxies selected in $(ugi)_s$ that are missed in *UVJ* lie in the region typically occupied by post-starbursts and young quiescent galaxies. Their SEDs and derived fit parameters (Figure 17) indicate that they are young (median age ∼0.5 Gyr) and have low dust extinction (median $A_V = 0.24$) and SFRs (median $\sim 3.8 M_\odot\,\mathrm{yr}^{-1}$). Due to their central wavelengths, the u_s and g_s filters are more sensitive to the Balmer break, which is strongest for galaxies that are 300–500 Myr old (D'Eugenio et al. 2021). The $U - V$ color, on the other hand, is more sensitive to the 4000 Å break, which becomes stronger than the Balmer break for populations that are ∼1 Gyr old.
2. The galaxies missed in $(ugi)_s$ selection are generally not quiescent. They span a larger range in age, dust extinction, and SFR than the above. However, they fall into two broad categories: (1) young (<0.5 Gyr) star-forming galaxies with low to moderate dust extinction ($A_V < 0.5$) and (2) old (>1 Gyr) star-forming galaxies with varying levels of dust. Although these galaxies are not selected in $(ugi)_s$ a number of them are selected in *UVJ* (Figure 18) and *ugi* (Figures 19 and 20). This suggests that we have underestimated our completeness rates, particularly for $(ugi)_s$ in Section 5.1.
3. The contaminants (FP) in $(ugi)_s$ are (1) old (>1 Gyr) galaxies with moderate ($A_V = 0.5$–0.8) dust extinction and little-to-no emission lines. (2) Those with strong emission lines (which are few) tend to be galaxies with large (∼10%–20%) photo-z uncertainties. (3) A handful of very young (<600 Myr) dusty ($A_V > 1$) star-forming galaxies also contaminate the $(ugi)_s$ quiescent region. (4) Galaxies with high dust extinction ($A_V > 2$) tend to cluster at $(u_s - g_s) > 2.4$; therefore, they may be culled using this criterion. (5) Catastrophic outliers ($\sigma_z > 50\%$) contaminate the quiescent region in all three methods.

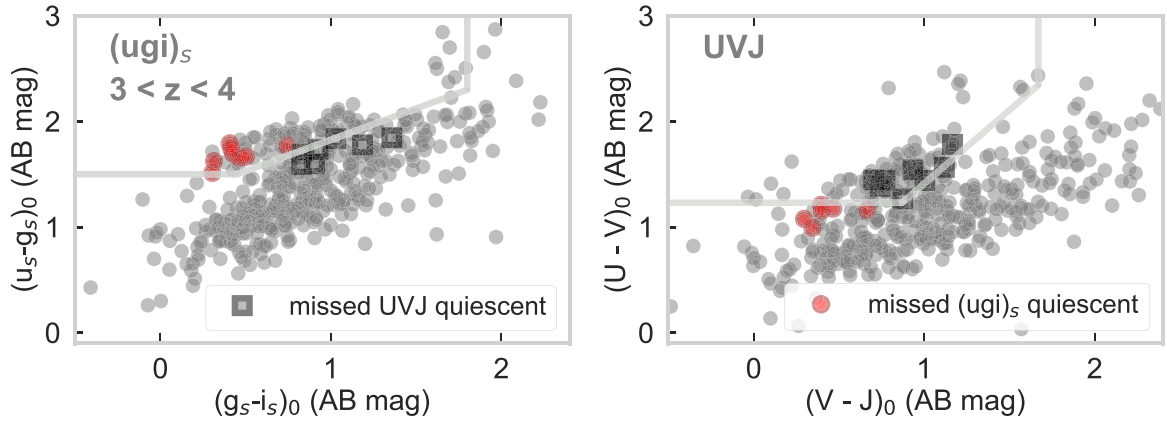

Figure 16. UltraVISTA galaxies with $\log(M/M_\odot) > 10.5$, at $3 < z < 4$, selected as quiescent in *UVJ* that are not selected in $(ugi)_s$ and vice versa. The $(ugi)_s$-selected quiescent galaxies that are missed in *UVJ* lie in the region typically occupied by post-starbursts and young quiescent galaxies. This is confirmed by their SEDs and derived stellar population parameters in Figure 17.

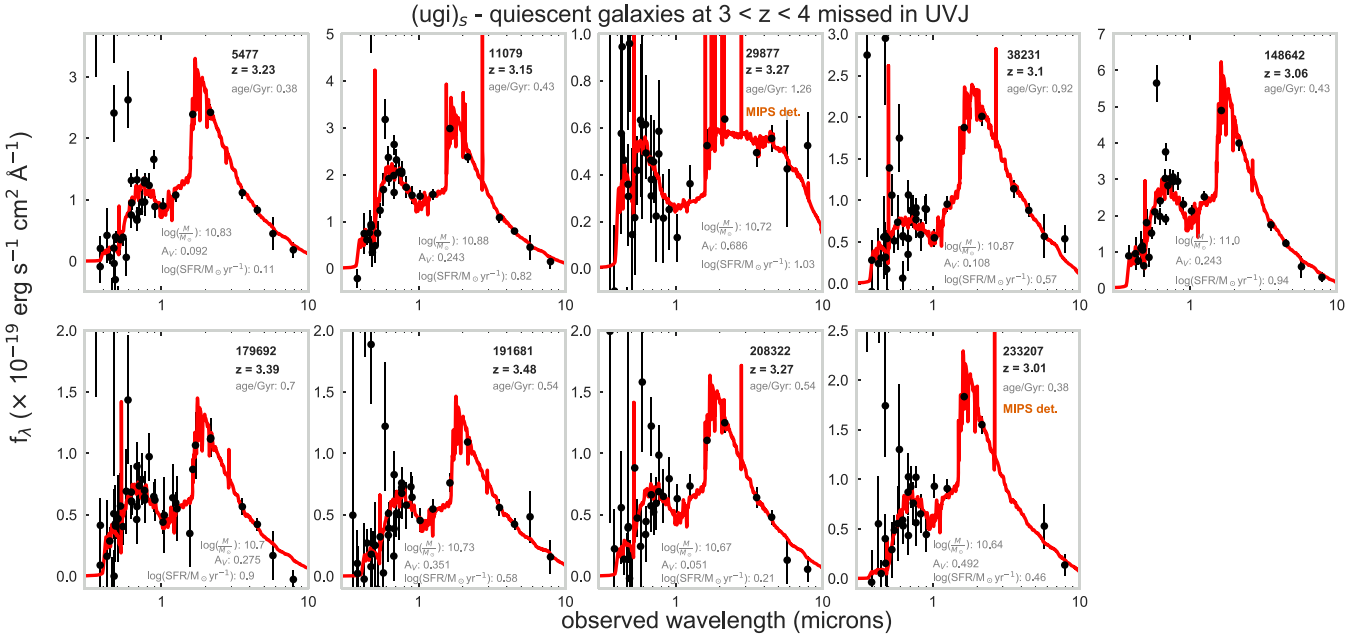

Figure 17. Best-fit SEDs and derived stellar population parameters of $(ugi)_s$-selected quiescent galaxies that are missed in *UVJ* selection at $3 < z < 4$ (red circles in Figure 16). Eight out of nine are young (400–900 Myr) galaxies with relatively low star formation rates ($<9\ M_\odot\ \mathrm{yr}^{-1}$) and dust extinction ($A_V < 0.5$). The exception (ID = 29877) was erroneously selected likely due to its high photometric redshift uncertainty ($\sigma_z \sim 25\%$). Galaxies detected at S/N > 3 in MIPS 24 μm emission are labeled in orange.

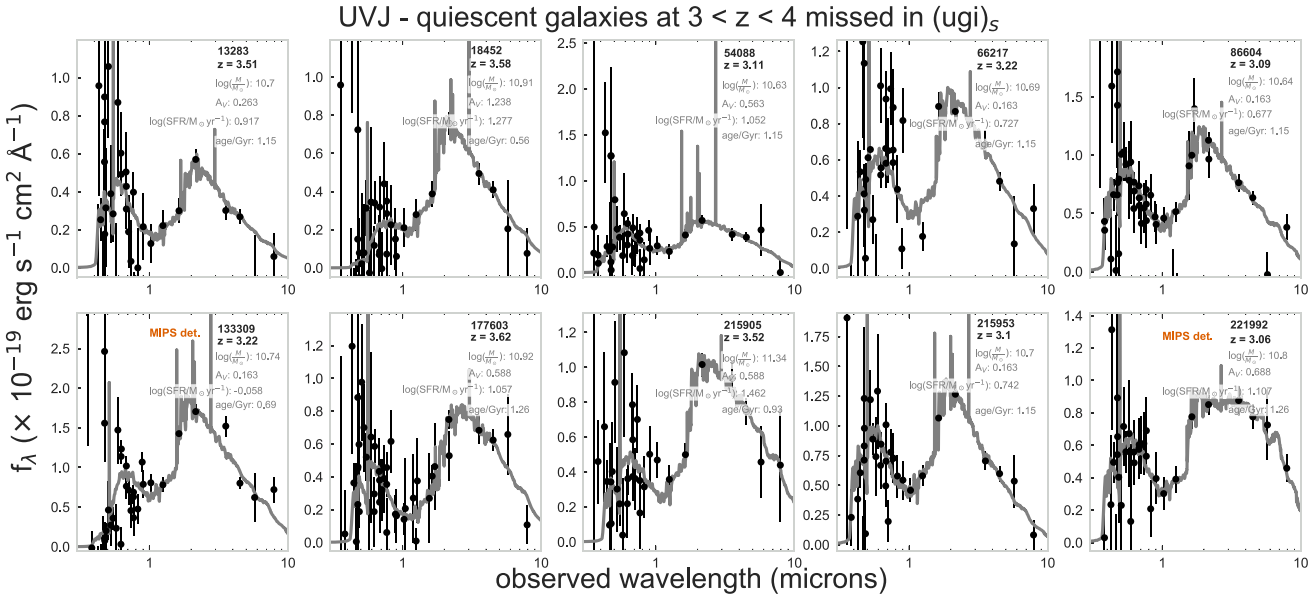

Figure 18. Best-fit SEDs and derived stellar population parameters of *UVJ*-selected quiescent galaxies that are missed in $(ugi)_s$ selection at $3 < z < 4$ (gray squares in Figure 16). These were erroneously selected likely due to emission-line contamination.

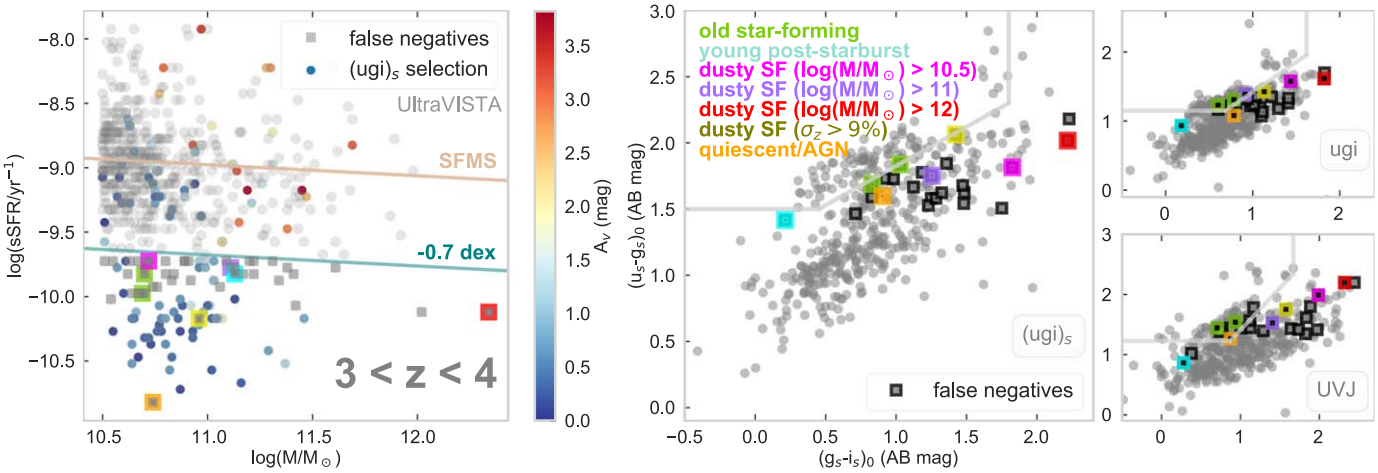

Figure 19. Left: demographics of $(ugi)_s$-selected quiescent galaxies at $3 < z < 4$ in UltraVISTA. Similar to Figure 9, we have color-coded these galaxies by their best-fit dust extinction values from MAGPHYS. The gray squares show *all* galaxies that were not selected as quiescent in $(ugi)_s$. Right: locations of false negatives in $(ugi)_s$, *ugi*, and *UVJ*. The SEDs of the highlighted false negatives (colored squares) are shown in Figure 20.

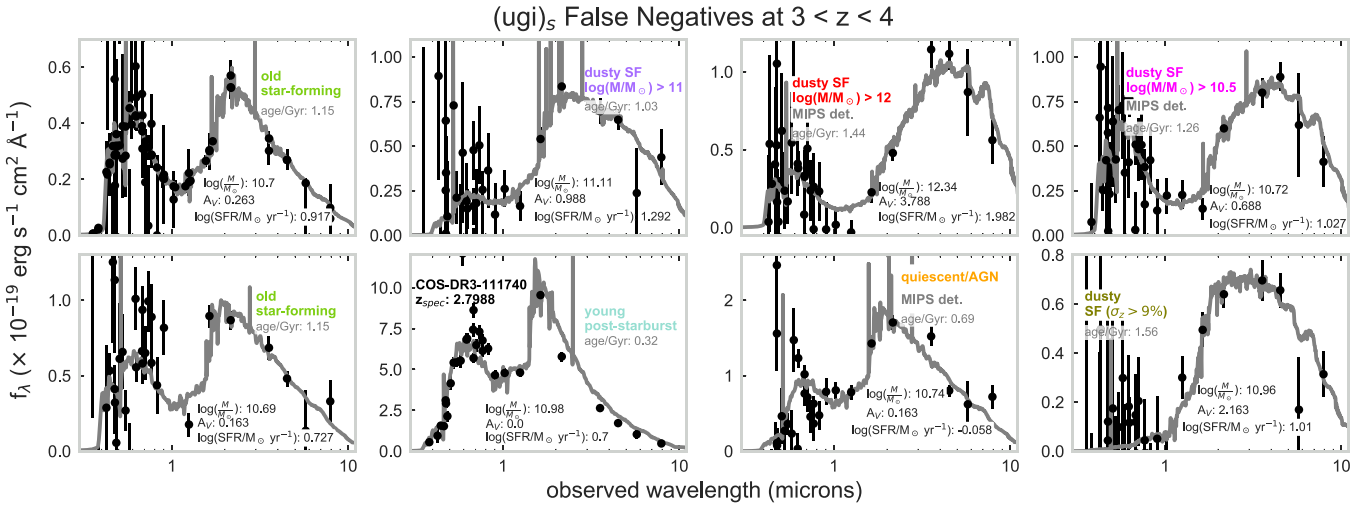

Figure 20. SEDs and stellar population parameters of low sSFR galaxies missed in $(ugi)_s$ selection at $3 < z < 4$. The SED and stellar population parameters of COS-DR3-111740 are based on fits to *Keck*/MOSFIRE spectra in Forrest et al. (2020a).

ORCID iDs

Jacqueline Antwi-Danso https://orcid.org/0000-0002-0243-6575
Casey Papovich https://orcid.org/0000-0001-7503-8482
Joel Leja https://orcid.org/0000-0001-6755-1315
Danilo Marchesini https://orcid.org/0000-0001-9002-3502
Z. Cemile Marsan https://orcid.org/0000-0002-7248-1566
Nicholas S. Martis https://orcid.org/0000-0003-3243-9969
Ivo Labbé https://orcid.org/0000-0002-2057-5376
Adam Muzzin https://orcid.org/0000-0002-9330-9108
Karl Glazebrook https://orcid.org/0000-0002-3254-9044
Caroline M. S. Straatman https://orcid.org/0000-0001-5937-4590
Kim-Vy H. Tran https://orcid.org/0000-0001-9208-2143

References

Akins, H. B., Narayanan, D., Whitaker, K. E., et al. 2022, ApJ, 929, 94
Arnouts, S., Walcher, C. J., Le Fevre, O., et al. 2007, A&A, 476, 137
Ashby, M. L. N., Willner, S. P., Fazio, G. G., et al. 2015, ApJS, 218, 33
Astropy Collaboration, Price-Whelan, A. M., Sipőcz, B. M., et al. 2018, AJ, 156, 123
Barro, G., Pérez-González, P. G., Cava, A., et al. 2019, ApJS, 243, 22
Beers, T. C., Flynn, K., & Gebhardt, K. 1990, AJ, 100, 32
Behroozi, P., Conroy, C., Wechsler, R. H., et al. 2020, MNRAS, 499, 5702
Behroozi, P. S., Conroy, C., & Wechsler, R. H. 2010, ApJ, 717, 379
Belfiore, F., Maiolino, R., Bundy, K., et al. 2018, MNRAS, 477, 3014
Belli, S., Newman, A. B., & Ellis, R. S. 2019, ApJ, 874, 17
Belli, S., Genzel, R., Förster Schreiber, N. M., et al. 2017, ApJL, 841, L6
Bouwens, R. J., Illingworth, G. D., Oesch, P. A., et al. 2015, ApJ, 803, 34
Boyett, K. N. K., Stark, D. P., Bunker, A. J., Tang, M., & Maseda, M. V. 2022, MNRAS, 513, 4451
Bradley, L. D., Bouwens, R. J., Zitrin, A., et al. 2012, ApJ, 747, 3
Bradley, L. D., Zitrin, A., Coe, D., et al. 2014, ApJ, 792, 76
Brammer, G. 2021, gbrammer/eazy-py: Tagged release 2021, Zenodo, doi:10.5281/zenodo.5012705
Brammer, G. B., van Dokkum, P. G., & Coppi, P. 2008, ApJ, 686, 1503
Brammer, G. B., Whitaker, K. E., van Dokkum, P. G., et al. 2009, ApJL, 706, L173
Brammer, G. B., Whitaker, K. E., van Dokkum, P. G., et al. 2011, ApJ, 739, 24
Bruzual, G., & Charlot, S. 2003, MNRAS, 344, 1000
Caliendo, J. N., Whitaker, K. E., Akhshik, M., et al. 2021, ApJL, 910, L7
Calzetti, D., Armus, L., Bohlin, R. C., et al. 2000, ApJ, 533, 682
Carnall, A. C., McLure, R. J., Dunlop, J. S., & Davé, R. 2018, MNRAS, 480, 4379
Carnall, A. C., McLure, R. J., Dunlop, J. S., et al. 2019, MNRAS, 490, 417
Carnall, A. C., Walker, S., McLure, R. J., et al. 2020, MNRAS, 496, 695
Casali, M., Adamson, A., Alves de Oliveira, C., et al. 2007, A&A, 467, 777

Castellano, M., Pentericci, L., Fontana, A., et al. 2017, ApJ, 839, 73
Chabrier, G. 2003, PASP, 115, 763
Chang, Y.-Y., van der Wel, A., da Cunha, E., & Rix, H.-W. 2015, ApJS, 219, 8
Charlot, S., & Fall, S. M. 2000, ApJ, 539, 718
Chevallard, J., & Charlot, S. 2016, MNRAS, 462, 1415
Cimatti, A., Daddi, E., Renzini, A., et al. 2004, Natur, 430, 184
Coe, D., Salmon, B., Bradač, M., et al. 2019, ApJ, 884, 85
Cohn, J. H., Leja, J., Tran, K.-V.-H., et al. 2018, ApJ, 869, 141
Conroy, C. 2013, ARA&A, 51, 393
Conroy, C., & Gunn, J. E. 2010, FSPS: Flexible Stellar Population Synthesis, Astrophysics Source Code Library, ascl:1010.043
Croux, C., & Rousseeuw, P. J. 1992, in Computational Statistics, ed. Y. Dodge & J. Whittaker (Heidelberg: Physica-Verlag HD), 411
da Cunha, E., Charlot, S., & Elbaz, D. 2008, MNRAS, 388, 1595
Cunha, E. d., Walter, F., Smail, I. R., et al. 2015, ApJ, 806, 110
Daddi, E., Cimatti, A., Renzini, A., et al. 2004, ApJ, 617, 746
D'Eugenio, C., Daddi, E., Gobat, R., et al. 2020, ApJL, 892, L2
D'Eugenio, C., Daddi, E., Gobat, R., et al. 2021, A&A, 653, A32
Díaz-García, L. A., Cenarro, A. J., López-Sanjuan, C., et al. 2019, A&A, 631, A156
Donnari, M., Pillepich, A., Nelson, D., et al. 2019, MNRAS, 485, 4817
Dunlop, J. S., Abraham, R. G., Ashby, M. L. N., et al. 2021, PRIMER: Public Release IMaging for Extragalactic Research, JWST Proposal. Cycle 1, ID. #1837
Ellis, R. S., McLure, R. J., Dunlop, J. S., et al. 2013, ApJL, 763, L7
Endsley, R., Stark, D. P., Chevallard, J., & Charlot, S. 2021, MNRAS, 500, 5229
Erfanianfar, G., Popesso, P., Finoguenov, A., et al. 2016, MNRAS, 455, 2839
Esdaile, J., Labbé, I., Glazebrook, K., et al. 2021, AJ, 162, 225
Fang, J. J., Faber, S. M., Koo, D. C., et al. 2018, ApJ, 858, 100
Finkelstein, S. L., Dickinson, M., Ferguson, H. C., et al. 2017, The Cosmic Evolution Early Release Science (CEERS) Survey, JWST Proposal ID 1345. Cycle 0
Forrest, B., Tran, K.-V.-H., Tomczak, A. R., et al. 2016, ApJL, 818, L26
Forrest, B., Marsan, Z. C., Annunziatella, M., et al. 2020a, ApJ, 903, 47
Forrest, B., Annunziatella, M., Wilson, G., et al. 2020b, ApJL, 890, L1
Freedman, D., & Diaconis, P. 1981, Zeitschrift für Wahrscheinlichkeitstheorie und Verwandte Gebiete, 57, 453
Glazebrook, K., Schreiber, C., Labbé, I., et al. 2017, Natur, 544, 71
Grogin, N. A., Kocevski, D. D., Faber, S. M., et al. 2011, ApJS, 197, 35
Guo, Y., Ferguson, H. C., Giavalisco, M., et al. 2013, ApJS, 207, 24
Gutkin, J., Charlot, S., & Bruzual, G. 2016, MNRAS, 462, 1757
Hainline, K. N., Hviding, R. E., Rieke, M., et al. 2020, ApJ, 892, 125
Harikane, Y., Inoue, A. K., Mawatari, K., et al. 2022, ApJ, 929, 1
Harris, C. R., Millman, K. J., van der Walt, S. J., et al. 2020, Natur, 585, 357
Heinis, S., Buat, V., Béthermin, M., et al. 2014, MNRAS, 437, 1268
Hunter, J. D. 2007, CSE, 9, 90
Hwang, Y.-H., Wang, W.-H., Chang, Y.-Y., et al. 2021, ApJ, 913, 6
Ilbert, O., Salvato, M., Le Floc'h, E., et al. 2010, ApJ, 709, 644
Ilbert, O., McCracken, H. J., Le Fèvre, O., et al. 2013, A&A, 556, A55
Ilbert, O., Arnouts, S., Le Floc'h, E., et al. 2015, A&A, 579, A2
Izotov, Y. I., Guseva, N. G., Fricke, K. J., & Henkel, C. 2016, MNRAS, 462, 4427
Johnson, B., & Leja, J. 2017, Bd-J/Prospector: Initial Release, v0.1, Zenodo, doi:10.5281/zenodo.1116491
Kalita, B. S., Daddi, E., D?Eugenio, C., et al. 2021, ApJL, 917, L17
Kartaltepe, J., Casey, C. M., Bagley, M., et al. 2021, COSMOS-Webb: The Webb Cosmic Origins Survey, JWST Proposal. Cycle 1, ID. #1727
Katsianis, A., Gonzalez, V., Barrientos, D., et al. 2020, MNRAS, 492, 5592
Kauffmann, O. B., Le Fèvre, O., Ilbert, O., et al. 2020, A&A, 640, A67
Kawinwanichakij, L., Quadri, R. F., Papovich, C., et al. 2016, ApJ, 817, 9
Kissler-Patig, M., Pirard, J.-F., Casali, M., et al. 2008, A&A, 491, 941
Kluyver, T., Ragan-Kelley, B., Pérez, F., et al. 2016, in Positioning and Power in Academic Publishing: Players, Agents and Agendas, ed. F. Loizides & B. Schmidt (Amsterdam: IOS Press), 87
Koekemoer, A. M., Faber, S. M., Ferguson, H. C., et al. 2011, ApJS, 197, 36
Kriek, M., van Dokkum, P. G., Labbé, I., et al. 2009, ApJ, 700, 221
Kriek, M., Labbé, I., Conroy, C., et al. 2010, ApJL, 722, L64
Kurczynski, P., Gawiser, E., Acquaviva, V., et al. 2016, ApJL, 820, L1
Labbé, I., Huang, J., Franx, M., et al. 2005, ApJL, 624, L81
Labbé, I., Oesch, P. A., Bouwens, R. J., et al. 2013, ApJL, 777, L19
Lee, N., Sanders, D. B., Casey, C. M., et al. 2015, ApJ, 801, 80
Lee, S.-K., Ferguson, H. C., Somerville, R. S., Wiklind, T., & Giavalisco, M. 2010, ApJ, 725, 1644
Leja, J., Carnall, A. C., Johnson, B. D., Conroy, C., & Speagle, J. S. 2019a, ApJ, 876, 3
Leja, J., Tacchella, S., & Conroy, C. 2019b, ApJL, 880, L9
Leja, J., Johnson, B. D., Conroy, C., Dokkum, P. G. v., & Byler, N. 2017, ApJ, 837, 170
Leja, J., van Dokkum, P. G., Franx, M., & Whitaker, K. E. 2015, ApJ, 798, 115
Leja, J., Johnson, B. D., Conroy, C., et al. 2019c, ApJ, 877, 140
Leja, J., Speagle, J. S., Ting, Y.-S., et al. 2022, ApJ, 936, 165
Lotz, J. M., Koekemoer, A., Coe, D., et al. 2017, ApJ, 837, 97
Lustig, P., Strazzullo, V., Remus, R.-S., et al. 2023, MNRAS, 518, 5953
Lutz, D., Poglitsch, A., Altieri, B., et al. 2011, A&A, 532, A90
Man, A. W. S., Greve, T. R., Toft, S., et al. 2016, ApJ, 820, 11
Marchesini, D., van Dokkum, P. G., Förster Schreiber, N. M., et al. 2009, ApJ, 701, 1765
Marchesini, D., Whitaker, K. E., Brammer, G., et al. 2010, ApJ, 725, 1277
Marsan, C., Muzzin, A., Alcorn, L. Y., et al. 2021, Dawn of the Monsters: JWST Characterization of Extremely Massive Galaxies at z 5, JWST Proposal. Cycle 1, ID. #2362
Marsan, Z. C., Marchesini, D., Brammer, G. B., et al. 2015, ApJ, 801, 133
Marsan, Z. C., Muzzin, A., Marchesini, D., et al. 2022, ApJ, 924, 25
Martin, D. C., Wyder, T. K., Schiminovich, D., et al. 2007, ApJS, 173, 342
Martis, N. S., Marchesini, D. M., Muzzin, A., et al. 2019, ApJ, 882, 65
Martis, N. S., Marchesini, D., Brammer, G. B., et al. 2016, ApJL, 827, L25
Maseda, M. V., van der Wel, A., Rix, H.-W., et al. 2018, ApJ, 854, 29
Mawatari, K., Yamada, T., Fazio, G. G., Huang, J.-S., & Ashby, M. L. N. 2016, PASJ, 68, 46
McCarthy, P. J., Le Borgne, D., Crampton, D., et al. 2004, ApJL, 614, L9
McCracken, H. J., Milvang-Jensen, B., Dunlop, J., et al. 2012, A&A, 544, A156
Merlin, E., Fontana, A., Castellano, M., et al. 2018, MNRAS, 473, 2098
Merlin, E., Fortuni, F., Torelli, M., et al. 2019, MNRAS, 490, 3309
Mitchell, P. D., Lacey, C. G., Baugh, C. M., & Cole, S. 2013, MNRAS, 435, 87
Mobasher, B., Dahlen, T., Ferguson, H. C., et al. 2015, ApJ, 808, 101
Moles, M., Benítez, N., Aguerri, J. A. L., et al. 2008, AJ, 136, 1325
Momcheva, I. G., Brammer, G. B., van Dokkum, P. G., et al. 2016, ApJS, 225, 27
Muzzin, A., Marchesini, D., van Dokkum, P. G., et al. 2009, ApJ, 701, 1839
Muzzin, A., Marchesini, D., Stefanon, M., et al. 2013, ApJ, 777, 18
Nanayakkara, T., Esdaile, J., Glazebrook, K., et al. 2022, PASA, 39, e002
Nayyeri, H., Mobasher, B., Hemmati, S., et al. 2014, ApJ, 794, 68
Oesch, P. A., Bouwens, R. J., Illingworth, G. D., Labbé, I., & Stefanon, M. 2018, ApJ, 855, 105
Oesch, P. A., Bouwens, R. J., Illingworth, G. D., et al. 2014, ApJ, 786, 108
Oke, J. B., & Gunn, J. E. 1983, ApJ, 266, 713
Oliver, S. J., Bock, J., Altieri, B., et al. 2012, MNRAS, 424, 1614
Pacifici, C., Kassin, S. A., Weiner, B. J., et al. 2016, ApJ, 832, 79
Pannella, M., Carilli, C. L., Daddi, E., et al. 2009, ApJL, 698, L116
Papovich, C., Dickinson, M., & Ferguson, H. C. 2001, ApJ, 559, 620
Papovich, C., Finkelstein, S. L., Ferguson, H. C., Lotz, J. M., & Giavalisco, M. 2011, MNRAS, 412, 1123
Papovich, C., Bassett, R., Lotz, J. M., et al. 2012, ApJ, 750, 93
Papovich, C., Labbé, I., Quadri, R., et al. 2015, ApJ, 803, 26
Papovich, C., Shipley, H. V., Mehrtens, N., et al. 2016, ApJS, 224, 28
Patel, S. G., Holden, B. P., Kelson, D. D., et al. 2012, ApJL, 748, L27
Patel, S. G., Hong, Y. X., Quadri, R. F., Holden, B. P., & Williams, R. J. 2017, ApJ, 839, 127
Persson, S. E., Murphy, D. C., Smee, S., et al. 2013, PASP, 125, 654
Pforr, J., Maraston, C., & Tonini, C. 2012, MNRAS, 422, 3285
Popesso, P., Morselli, L., Concas, A., et al. 2019, MNRAS, 490, 5285
Price, S. H., Kriek, M., Brammer, G. B., et al. 2014, ApJ, 788, 86
Quadri, R., Marchesini, D., van Dokkum, P., et al. 2007, AJ, 134, 1103
Rasappu, N., Smit, R., Labbé, I., et al. 2016, MNRAS, 461, 3886
Reddy, N. A., Pettini, M., Steidel, C. C., et al. 2012, ApJ, 754, 25
Reddy, N. A., Shapley, A. E., Sanders, R. L., et al. 2018, ApJ, 869, 92
Renzini, A., & Peng, Y.-j. 2015, ApJL, 801, L29
Roberts-Borsani, G. W., Bouwens, R. J., Oesch, P. A., et al. 2016, ApJ, 823, 143
Robertson, B. E. 2022, ARA&A, 60, 121
Rodighiero, G., Renzini, A., Daddi, E., et al. 2014, MNRAS, 443, 19
Roebuck, E., Sajina, A., Hayward, C. C., et al. 2019, ApJ, 881, 18
Salim, S., Charlot, S., Rich, R. M., et al. 2005, ApJL, 619, L39
Salmon, B., Coe, D., Bradley, L., et al. 2018, ApJL, 864, L22
Sanders, D. B., Salvato, M., Aussel, H., et al. 2007, ApJS, 172, 86
Santini, P., Ferguson, H. C., Fontana, A., et al. 2015, ApJ, 801, 97
Santini, P., Castellano, M., Merlin, E., et al. 2021, A&A, 652, A30
Saracco, P., Marchesini, D., Barbera, F. L., et al. 2020, ApJ, 905, 40
Schawinski, K., Urry, C. M., Simmons, B. D., et al. 2014, MNRAS, 440, 889

Schmidt, K. B., Treu, T., Trenti, M., et al. 2014, ApJ, 786, 57
Schreiber, C., Pannella, M., Elbaz, D., et al. 2015, A&A, 575, A74
Schreiber, C., Glazebrook, K., Nanayakkara, T., et al. 2018, A&A, 618, A85
Seabold, S., & Perktold, J. 2010, in 9th Python in Science Conf., 92
Shahidi, A., Mobasher, B., Nayyeri, H., et al. 2020, ApJ, 897, 44
Shapley, A. E., Steidel, C. C., Erb, D. K., et al. 2005, ApJ, 626, 698
Shen, X., Vogelsberger, M., Nelson, D., et al. 2020, MNRAS, 495, 4747
Sherman, S., Jogee, S., Florez, J., et al. 2021, MNRAS, 505, 947
Skelton, R. E., Whitaker, K. E., Momcheva, I. G., et al. 2014, ApJS, 214, 24
Smit, R., Bouwens, R. J., Labbé, I., et al. 2014, ApJ, 784, 58
Smit, R., Bouwens, R. J., Franx, M., et al. 2015, ApJ, 801, 122
Smith, M. W. L., Eales, S. A., Gomez, H. L., et al. 2012, ApJ, 756, 40
Sobral, D., Best, P. N., Smail, I., et al. 2014, MNRAS, 437, 3516
Speagle, J. S., Steinhardt, C. L., Capak, P. L., & Silverman, J. D. 2014, ApJS, 214, 15
Spitler, L. R., Straatman, C. M. S., Labbé, I., et al. 2014, ApJL, 787, L36
Springel, V., Pakmor, R., Pillepich, A., et al. 2018, MNRAS, 475, 676
Steinborn, L. K., Dolag, K., Comerford, J. M., et al. 2016, MNRAS, 458, 1013
Steinhardt, C. L., Weaver, J. R., Maxfield, J., et al. 2020, ApJ, 891, 136
Straatman, C. M. S., Labbé, I., Spitler, L. R., et al. 2014, ApJL, 783, L14
Straatman, C. M. S., Spitler, L. R., Quadri, R. F., et al. 2016, ApJ, 830, 51
Strom, A. L., Steidel, C. C., Rudie, G. C., et al. 2017, ApJ, 836, 164
Sutherland, W., Emerson, J., Dalton, G., et al. 2015, A&A, 575, A25
Tacchella, S., Carollo, C. M., Förster Schreiber, N. M., et al. 2018, ApJ, 859, 56
Tacchella, S., Conroy, C., Faber, S. M., et al. 2022, ApJ, 926, 134
Tal, T., Dekel, A., Oesch, P., et al. 2014, ApJ, 789, 164
Tanaka, M., Valentino, F., Toft, S., et al. 2019, ApJL, 885, L34
Tang, M., Stark, D. P., Chevallard, J., et al. 2021, MNRAS, 501, 3238
Tasca, L. A. M., Le Fèvre, O., Hathi, N. P., et al. 2015, A&A, 581, A54
The Pandas Development Team 2020, pandas-dev/pandas: Pandas, latest, Zenodo, doi:10.5281/zenodo.3509134
Tomczak, A. R., Quadri, R. F., Tran, K.-V.-H., et al. 2014, ApJ, 783, 85
Tomczak, A. R., Quadri, R. F., Tran, K.-V.-H., et al. 2016, ApJ, 817, 118
Tran, K.-V.-H., Forrest, B., Alcorn, L. Y., et al. 2020, ApJ, 898, 45
Valentino, F., Tanaka, M., Davidzon, I., et al. 2020, ApJ, 889, 93
van der Wel, A., Straughn, A. N., Rix, H.-W., et al. 2011, ApJ, 742, 111
Virtanen, P., Gommers, R., Oliphant, T. E., et al. 2020, NatMe, 17, 261
Waskom, M. 2021, JOSS, 6, 3021
Weaver, J. R., Kauffmann, O. B., Ilbert, O., et al. 2022, ApJS, 258, 11
Whitaker, K. E., Labbé, I., van Dokkum, P. G., et al. 2011, ApJ, 735, 86
Whitaker, K. E., van Dokkum, P. G., Brammer, G., et al. 2013, ApJL, 770, L39
Whitaker, K. E., Franx, M., Leja, J., et al. 2014, ApJ, 795, 104
Whitaker, K. E., Narayanan, D., Williams, C. C., et al. 2021a, ApJL, 922, L30
Whitaker, K. E., Williams, C. C., Mowla, L., et al. 2021b, Natur, 597, 485
Williams, C. C., Curtis-Lake, E., Hainline, K. N., et al. 2018, ApJS, 236, 33
Williams, C. C., Spilker, J. S., Whitaker, K. E., et al. 2021, ApJ, 908, 54
Williams, R. J., Quadri, R. F., Franx, M., van Dokkum, P., & Labbe, I. 2009, ApJ, 691, 1879
Williams, R. J., Quadri, R. F., Franx, M., et al. 2010, ApJ, 713, 738
Wold, I. G. B., Kawinwanichakij, L., Stevans, M. L., et al. 2019, ApJS, 240, 5
Wolf, C., Aragon-Salamanca, A., Balogh, M., et al. 2009, MNRAS, 393, 1302
Wuyts, S., Franx, M., Cox, T. J., et al. 2009, ApJ, 696, 348
Wuyts, S., Förster Schreiber, N. M., Genzel, R., et al. 2012, ApJ, 753, 114